Probing the southern African lithosphere with magnetotellurics, Part I, model construction

Max Moorkamp[1], Sinan Özaydın[2], Kate Selway[2,3,4], Alan G. Jones[5]

[1]Ludwig-Maximilians-Universität, Department of Earth and Environmental Sciences, Theresienstrasse 41, 80333 Munich, Germany

[2]Macquarie University, ARC Centre of Excellence for Core to Crust Fluid Systems (CCFS), Department of Earth and Environmental Sciences, Sydney, Australia

[3]University of South Australia, Future Industries Institute, Australia

[4]University of Oslo, Centre for Earth Evolution and Development (CEED), Norway

[5]Complete MT Solutions Inc., Ottawa, Canada; formerly Dublin Institute for Advanced Studies, Dublin, Ireland

Key Points:

- We create the first large-scale conductivity models of southern Africa.
- We compare different strategies to construct continental scale models and investigate the impact on the results.
- The main inversion features are common to all models, with most differences being due to regularization.

Corresponding author: Max Moorkamp, Max.Moorkamp@lmu.de

Abstract

The Southern African Magnetotelluric Experiment (SAMTEX) involved the collection of data at over 700 sites in Archean to Proterozoic southern Africa, spanning features including the Kalahari Craton, Bushveld Complex and voluminous kimberlites. Here, we present the first 3D inversions of the full SAMTEX dataset. In this paper, we focus on assessing the robustness of the 3D models by comparing two different inversion codes, *jif3D* and *ModEM*, and two different subsets of the data, one containing all acceptable data and the other containing a smaller selection of undistorted, high-quality data. Results show that the main conductive and resistive features are imaged by all inversions, including deep resistive features in the central Kaapvaal Craton and southern Congo Craton and a lithospheric-scale conductor beneath the Bushveld Complex. Despite this, differences exist between the *jif3D* and *ModEM* inverse models that derive mainly from the differences in regularization between the models, with *jif3D* producing models that are very smooth laterally and with depth, while *ModEM* produces models with more discrete conductive and resistive features. Analysis of the differences between these two inversions can provide a good indication of the model resolution. More minor differences are apparent between models run with different subsets of data, with the models containing all acceptable data featuring higher wavelength conductivity variations than those run with fewer stations but also demonstrating poorer data fit.

Plain Language Summary

We investigate the structure of the upper 200 km of the Earth beneath southern Africa. To achieve this, we utilize an electromagnetic geophysical technique called magnetotellurics which is sensitive to variations in electrical resistivity within the Earth. To reconstruct electrical resistivity from magnetotelluric measurements, we use so-called inversion algorithms. However, the results are non-unique and a variety of different parameters have to be chosen by the user during the inversion process. In order to better understand the possible variability in our Earth models, we use different inversion algorithms and compare different strategies. This allows us to assess the reliability of our results. Based on our models and their comparison, we infer that the lithosphere, the solid outer shell of the Earth, varies in thickness below our study area and is thickest below central South Africa. In addition, we can detect remnants of past continental col-

lisions that have been preserved for hundreds of millions of years since this part of the world was assembled from the collision of various micro-continents.

1 Introduction

The lithosphere of southern Africa is among the most important in the world for understanding continental evolution (e.g., Lee et al., 2011). It contains extensive, Archean to Paleoproterozoic cratons, including the Kaapvaal, Zimbabwe and Congo cratons, which are also sampled by voluminous kimberlite magmatism (e.g., De Wit et al., 1992; Begg et al., 2009). Investigations of the geological, geochemical and geophysical nature of these cratons help us understand the formation and amalgamation of the Archean continental lithosphere and the survival of that lithosphere to the present. The southern African lithosphere also hosts many of the world's largest mineral deposits (Clifford, 1966), including the world's largest platinum group element deposits in the Bushveld Complex (itself the world's largest layered mafic intrusion (e.g., VanTongeren, 2018)), extensive kimberlite-hosted diamond deposits including the Kimberley, Venetia and Jwaneng deposits (e.g., Field et al., 2008), and giant orogenic and placer gold deposits such as those in the Barberton Goldfields and Witwatersrand Basin (e.g., de Ronde & de Wit, 1994). Since the formation of many of these deposits involved lithospheric-scale processes, defining the lithospheric architecture and composition of southern Africa not only helps our understanding of continental evolution but also aids mineral exploration.

Analysis of the vast mantle xenolith and xenocryst databases has shown spatially and temporally complex patterns of depletion and metasomatism of the southern African mantle (e.g., Griffin et al., 2003; Kobussen et al., 2009; Grégoire et al., 2003). In some cratonic regions, inferences from xenoliths and seismic data can seem contradictory. Many xenoliths have metasomatised and geochemically fertile compositions, while seismic tomography models tend to show fast wave speeds extending to depths >200 km and have been interpreted to represent deep, geochemically depleted lithospheric keels (e.g., Fouch et al., 2004; White-Gaynor et al., 2020). This apparent contradiction has led to the suggestion that cratonic mantle xenoliths and xenocrysts from southern Africa may be unrepresentative of the cratonic mantle more generally (Griffin et al., 2009). In contrast, seismic receiver function data image several low-velocity anomalies within those southern African lithospheric keels, which indicate that broad metasomatism may be more widespread than suggested by the tomographic models (Sodoudi et al., 2013; Selway et al., 2015).

Here and in the accompanying manuscript, we add new magnetotelluric (MT) constraints to understanding the architecture, composition and evolution of the southern African lithosphere. MT data are sensitive to mantle metasomatism, both through the hydration of nominally anhydrous mantle minerals and through the precipitation of metasomatic minerals (e.g., Selway, 2014), and MT interpretations are generally consistent with mantle xenolith and xenocryst compositions (Özaydın et al., 2021). Therefore, MT models of southern Africa can provide new insights into the composition and metasomatism of the lithosphere. To do this, we have analysed and inverted the Southern African Magnetotelluric Experiment (SAMTEX) database (Jones et al., 2009). These data were collected between 2003–2008 and comprise more than 700 MT stations including broadband MT (BBMT) and long-period MT (LMT) measurements along more than 15,000 line km crossing South Africa, Botswana and Namibia.

In this paper, we describe the first 3D MT models of the entire SAMTEX dataset. In contrast to when SAMTEX was collected, 3D MT inversions are now routine. However, different inversion codes use different regularizations, model discretizations and forward modelling approaches, and the impact of these differences is not well understood. Therefore, we have inverted the dataset with two different algorithms *jif3D* (Moorkamp et al., 2011) and *ModEM* (Kelbert et al., 2014)) to compare results and ensure only the most robust features are interpreted. In the accompanying paper, we interpret the models in terms of the composition and evolution of the southern African lithospheric mantle.

2 The SAMTEX magnetotelluric dataset

Magnetotellurics (MT) is a passive electromagnetic technique to infer the resistivity of the subsurface from measurements at the surface (Chave & Jones, 2012). Together with seismic tomography and potential field methods (e.g., gravity, magnetics), MT is one of the foremost geophysical techniques to image the structure of the lithosphere-asthenosphere system. It has been used to investigate continental lithospheric structures in many regions around the world (e.g., Jones, 1999; Gatzemeier & Moorkamp, 2005; Rao et al., 2014; Wannamaker et al., 2017; Selway, 2018) and has been a component of large national programs in the United States (Kelbert, 2019), Australia (Kirkby et al., 2020) and China (S.-W. Dong et al., 2013). Based on simultaneous measurements of naturally occurring

variations of the electric field **E** and the magnetic field **B** we can estimate the frequency-dependent, complex-valued magnetotelluric impedance **Z**, viz.

$$\mathbf{E} = \mathbf{ZB}. \tag{1}$$

This estimation process is based on robust statistical methods and thus gives formal estimates of data uncertainties (e.g., Chave & Thomson, 2003) although these are typically increased before use in an inversion algorithm (e.g., Miensopust, 2017, and discussion below).

The MT response estimates used for our inversions were acquired during the Southern African Magnetotelluric Experiment (SAMTEX) between 2003–2008 (Jones et al., 2009). They comprise more than 700 broadband MT (BBMT) and long-period MT (LMT) measurements across South Africa, Botswana and Namibia. The primary goal of SAMTEX was to image the lithospheric architecture of the cratons and mobile belts in the region, and thus measurements were taken at intervals of roughly 20 km and at periods 0.01 - 10,000 s for the BBMT sites, and 60 km at 10 s - 10,000 s for the LMT sites. Due to long recording times and favourable noise conditions in many parts of the study area, the data quality at many sites is excellent throughout the period range. To date there have been a number of publications performing modelling and inversions for different subregions and profiles (Hamilton et al., 2006; Muller et al., 2009; Miensopust et al., 2011; Evans et al., 2011; Khoza et al., 2013; Finn et al., 2015; Moorkamp et al., 2019). In addition, maps of resistivity directly derived from the data at selected periods have been used to investigate the structure and composition of the lithosphere-asthenosphere system (Jones et al., 2012, 2013) and multi-observable petrological-geophysical models have been created based on subsets of the data (Fullea et al., 2011). Still, to date, no three-dimensional resistivity models of the lithosphere based on all the available data have been published.

We show representative data from six stations across the array in Figure 2. Their locations are shown as yellow stars in Figure 1. We concentrate on the period range of 1–10,000 s as lithospheric-scale structures are the focus of our modelling efforts. The sites show good data quality throughout the plotted period range, although at the longest periods ($> 1,000$ s), the scatter and error estimates increase at some of the sites (e.g., KAP45). The off-diagonal apparent resistivity sounding curves highlight a moderately conductive

shallow subsurface ($\approx$ 10 Ωm at short periods) at the northern sites RAK011A and ZIM117. Further south, at sites KIM428 and KAL014, the short period apparent resistivities are generally comparable but slightly higher, while the southernmost sites, KAP045 and KAP019, show significantly higher short period apparent resistivities of $\geq$ 500 Ωm. Beneath this surface layer, the sounding curves of the four northern sites suggest that resistivity increases with depth to a maximum of $\approx$ 500 Ωm at $\approx$ 500 s, before either remaining constant or decreasing slightly at longer periods. In contrast, at the two southern sites (KAP45 and KAP19), most of the apparent resistivity curves have higher initial values and decrease with period.

3 Inversions

3.1 Inversion Algorithms

We invert the observed MT impedances with two different inversion algorithms (Moorkamp et al., 2011; Kelbert et al., 2014) and two different strategies for each code. This helps us to address model uncertainties related to algorithm-specific choices, such as regularization, error floor, model discretization, and precision of the forward modelling engine. As a result of these choices, each code will fit different aspects of the data, including those affected by noise, to different degrees. As both algorithms used here are well established, we only give a brief summary of each algorithm and focus on comparing the differences and the potential impact on the results.

For two inversions, we use the MT inversion module of the joint inversion framework *jif3D* (Moorkamp et al., 2011). The numerical basis of the forward modelling engine and the gradient calculation are presented in Avdeev & Avdeeva (2009) and Avdeeva et al. (2015). It utilizes an integral-equation based forward engine *x3d* (Avdeev et al., 1997) and includes a correction for galvanic distortion at each site (Avdeeva et al., 2015; Moorkamp et al., 2020). Galvanic distortion of magnetotelluric impedances is typically caused by charge accumulation at small structures (compared to the induction length scale), and it can mathematically be described as a site-specific, frequency-independent multiplication of the impedances with a real-valued matrix $\mathbf{C}$ (Chave & Jones, 2012). In *jif3D* distortion correction is achieved by estimating the elements of $\mathbf{C}$ as part of the inversion and multiplying the synthetic impedance $\mathbf{Z}_{synth}$ at each site with the corre-

sponding distortion matrix when calculating the data misfit. Details on this methodology can be found in Avdeeva et al. (2015).

The inversion algorithm has been used on a range of MT datasets, both commercial and academic, including imaging the fault structure for an intra-plate event in Botswana (Moorkamp et al., 2019) and hydrothermal fluids in the central Andes (Pearce et al., 2020). Due to the integral equation based forward modelling algorithm, the horizontal cell sizes need to be constant in both orthogonal horizontal directions. In the vertical direction, cell sizes can vary and are typically fine near the surface, increasing by a constant factor with depth to match the decreasing resolution of MT data. The discretized region is embedded in a layered half-space that is kept constant throughout the inversion. Some care must be taken to avoid the strong influence of this background conductivity structure on the inversion results. In order to enforce positive conductivity values during optimization and restrict model conductivities to realistic values, conductivities in each model cell are transformed using the generalized model parameter scheme described in Moorkamp et al. (2011). This allows us to use an unconstrained optimization algorithm based on a limited-memory quasi-Newton method (L-BFGS, Avdeeva & Avdeev, 2006) to minimize the objective function. Within *jif3D* we regularize the inversion through a first-order approximation of the spatial gradient of the generalized model parameters. This approach has the advantage of equalizing the vast range of Earth conductivities ($\approx 10^{-1}$ to 10^{6} Ωm) to a range between approximately -2 and 2, and ensuring that the regularization operates similarly in all parts of the model. As the regularization is purely smoothness based, it has the potential disadvantage that structures may horizontally or vertically smear into regions of low resolution, such as those with poor site coverage in the heterogeneous SAMTEX array. However, this could be considered a form of natural interpolation.

The other two inversions were performed using *ModEM*, a well-established and freely available 3D MT inversion code (Egbert & Kelbert, 2012; Kelbert et al., 2014). It is widely used in the academic community and has seen applications on datasets around the world (e.g., Kelbert & Egbert, 2012; Meqbel et al., 2014; H. Dong et al., 2020; Robertson et al., 2020). Its forward engine is based on a finite-difference formulation (e.g., Mackie et al., 1994; Egbert & Kelbert, 2012) and its modular structure allows for inversion of different combinations of electromagnetic data (e.g., Campanya et al., 2016). Compared to *jif3D* the gridding requirements are less strict with variable-sized rectilinear cells in

all three coordinate directions. Furthermore, no background layered half-space is prescribed; instead, the grid must be extensive enough that secondary electromagnetic fields are insignificant at the model boundaries. Thus, a typical strategy for designing inversion grids in *ModEM* is to use an inner core with constant horizontal cell size and padding cells of increasing size around it. In *ModEM* the natural logarithm of conductivity is used as a model parameter which enforces positivity of conductivity and has an equalizing effect similar to the generalized model parameters in *jif3D*. *ModEM* does not allow the range of permitted conductivities to be directly limited, but the regularization limits the difference from a prior model, often the starting model, and lateral variations of conductivity simultaneously (Egbert & Kelbert, 2012). Compared to a pure smoothing-based regularization, this combined approach should reduce smearing but can result in artificial changes in conductivity if the prior model is not representative of the average conductivity in the region. In this case, poorly-resolved regions of the model will be kept at prior conductivity values, whereas well-resolved regions will exhibit a different conductivity.

3.2 Data selection

Within each inversion algorithm, we ran an "all data" inversion of the entire SAMTEX dataset (with only clearly erroneous stations removed) and another "selected" inversion of a subset of the data. This approach was designed to test the impacts of heterogeneous station coverage and of noisy and distorted data on the results of each inversion algorithm.

SAMTEX station coverage is highly heterogeneous compared to other large-scale initiatives such as USArray (Kelbert, 2019) or AusLAMP (e.g., Robertson et al., 2016; Kirkby et al., 2020; Thiel et al., 2020). Due to logistical constraints and the still prevalent two-dimensional inversion approaches at the time of planning the measurements, data were collected in relatively dense transects separated by significant gaps. In a 3D regional model, the crustal structure will therefore be strongly represented in the data near those profiles and completely absent in regions without coverage. In contrast, deeper features (50-200 km) will at least be partially sensed by the data even in regions without direct station coverage. For this reason, the focus of our inversions will largely be on the regional imaging of the mantle lithosphere-asthenosphere system. To image the mantle, dense sampling along the profiles could be either beneficial or detrimental. On the one

hand, dense coverage should result in redundant information and thus reduce the influence of noise for deep imaging, but on the other hand, dense measurements can be highly affected by local structures that cannot be represented well in the regional model. This issue might be further exacerbated by the need to choose a global regularization parameter for the model, as localized structures in densely covered areas might require a small regularization parameter. However, small regularization parameters might be inappropriate for regions without dense coverage.

The noise levels of SAMTEX data are also heterogeneous (Figure 3). Some sites show significant noise across the whole period range, with either highly scattered or physically unrealistic data (e.g., ELG010A). These sites were excluded from all inversions. Of the remaining sites, some (e.g., BOT405) display smooth sounding curves with phases in quadrant but also demonstrate large offsets between the apparent resistivity curves, indicating local static distortion. Others (e.g., KAP047 and WIN011) show similar signs of static distortion and additionally display rapidly varying phases that extend out of the quadrant, which could indicate local noise or strong resistivity contrasts in the shallow subsurface. Even though *jif3D* can correct for distortion and strategies have been devised for *ModEM* to mimic the effects of distortion (Meqbel et al., 2014), it is unclear to what degree the information from these sites is useful to constrain deep structures and whether fitting distorted sites prevents fitting other data. To investigate the impact of such sites, they were therefore retained in the "all data" inversion but excluded from the "selected" inversion. To further reduce station density and to assess the impact of heterogeneous station coverage, additional stations with low-quality long-period data ($> 500-10000\,s$) were also removed. After the selection procedure, the resulting "selected" dataset has a station spacing along the station transects of $\sim 30-80$ km in most regions, compared to ~ 20 km for the "all data" dataset (compare blue and red dots in Figure 1).

3.3 Inversion Setup

To be able to accommodate the entire region in a single model with acceptable computational run times, the horizontal discretization for the core region was chosen to be 15 km in the northing and easting directions for all inversions. Including the padding cells for the runs with *ModEM*, the inversion domain comprises $132\times133\times53$ cells with a vertical discretization of 50 m for the topmost cells increasing up 141 km at the bottom of the domain. Information on ocean bathymetry was introduced from the ETOPO1

global topographic dataset, and seawater was assigned a resistivity of 0.3 Ωm. On land, no topography was considered, and a starting resistivity of 100 Ωm was assigned to all cells.

Inversions for *ModEM* were run with error floors of 5% of $\sqrt{Z_{xy}Z_{yx}}$ on all tensor elements. The starting λ was set to 10 and decreased by a factor of 5 when the inversion when RMS misfit difference is less than 0.002. An isotropic smoothing operator was constructed with the covariance matrix set to 0.4 in all directions. For the inversions with *jif3D*, we used the same error floor as for the inversions with *ModEM*. We removed the outer padding cells from the grid used for modelling in *ModEM* resulting in a mesh with $119 \times 120 \times 48$ cells and chose a fixed background resistivity of 100 Ωm.

The inversions for *jif3D* were run with a similar approach to regularization as the inversions with ModEM. However we used different values for the regularization parameter, staring with $\lambda = 1,000$ and reducing it to $\lambda = 1$ in the final iterations, since the influence of the regularization on the inversion is different between the two algorithms. The initial iterations did not include any distortion correction, but this was enabled after the first regularization change as this has been shown to yield stable results (Moorkamp et al., 2020).

4 Data fit

For the selected datasets the inversion algorithms reach a final RMS of 1.7 (*jif3D*) and 2.3 (*ModEM*) after 200 and 146 inversion iterations, respectively. For the inversion of the full datasets, the corresponding RMS values are 2.7 and 5.0, respectively. We show the final root-mean-square (RMS) misfit at each site for all frequencies in Figure 5. When we only invert the selected data (bottom row) using both *jif3D* and *ModEM* we achieve a relatively homogeneous RMS between 1.5 and 2.5 at the majority of sites, and only a few sites exceed RMS values of 4.5. While there are some differences in how well sites are fit, the overall pattern is comparable and some sites are fit better in one inversion or the other. In contrast, when inverting the maximum amount of data, the distribution of RMS becomes much more heterogeneous. Many sites are still in the 1.5 to 2.5 range, but some sites exceed RMS values of 10. This effect appears to be more pronounced for *ModEM* than *jif3D* and some sites that were fit well in the "selected" inversion are now fitted significantly worse. These observations confirm that some data that were excluded

are, in fact, problematic for the inversion. At least for some of these sites, the distortion correction used by *jif3D* helps to achieve a better fit. The question remains, though, to which degree this impacts the final models.

Figure 4 shows the estimated values of the distortion matrix $\mathbf{C}$ for the two *jif3D* inversions at the central area of the array around the sites BOT405 and KAP047 (Figure 3) that were previously identified as distorted (a version with all stations can be found in the supplementary material). For the selected data inversion, $\mathbf{C}$ is close to the identity matrix at virtually all sites indicating little to no galvanic distortion. This demonstrates that the data selection process successfully removed stations with significant distortion and that the inversion algorithm does not introduce artificial distortion, for example, to achieve a low data misfit with a smooth model. When inverting the complete data set, some but not all of the additional sites show significant distortion and sites BOT405 and KAP047 are among the most distorted (Figure 4).

In theory, if galvanic distortion is caused by structures that are small compared to the typical induction scale length at short periods (Chave & Jones, 2012) and the distortion correction only represents this structure-related distortion, the estimates of $\mathbf{C}$ at neighbouring sites should show little correlation. Although this is the case in some regions, we also see clusters of sites with very similar distortion estimates, e.g., south of site BOT405. Here the estimate of C_{xx} is consistently larger than unity and C_{yy} smaller than unity at most sites. There are two possible explanations for this phenomenon: a) It is possible that these sites were all installed in similar geological conditions, for example, when looking for softer ground in an environment dominated by outcropping bedrock. b) More likely, the distortion estimates capture variability in structures that can, in principle, be resolved by MT measurements but cannot be represented by the chosen horizontal discretization of 15 km, i.e. they account for the so-called model discrepancy (Kennedy & O'Hagan, 2001). These stations are located at the northern end of the Kaapvaal Craton crossing into the Magondi Mobile Belt, and thus it is likely that significant deformation is recorded in the crust.

We compare the data fit for the distorted site BOT405 and and the exemplary sites RAK011A, KIM428 and KAP045 for the *ModEM* "all data" inversion (Figure 6) and the *jif3D* "all data" inversion (Figure 7). The difference between observed and predicted data for site BOT405 clearly shows how the distortion correction in *jif3D* helps to achieve

a better fit to the off-diagonal apparent resistivity curves. Whereas the model response from *ModEM* converges to a common apparent resistivity value at short periods, *jif3D* reproduces the constant offset between the two curves. Interestingly, although the off-diagonal phases are fit differently by both inversions, there is no clearly superior fit by either of the two models. At sites RAK011A and KIM428, both models produce virtually identical responses for the off-diagonal apparent resistivities and phases and match the observed data well. At site KIM428, the models reproduce all variations of the curves, while at site RAK011A, the overall shape is reproduced well by the models, but the phase anomaly in the xy-component at periods between 50-100 s is not fully reproduced by either model. At both stations, the diagonal elements are significantly smaller than the off-diagonal elements and are matched better by the *jif3D* inversion than the *ModEM* inversion. It is our experience that distortion correction helps to match diagonal elements better even when these are small (Moorkamp et al., 2020). The data at site KAP045 are matched differently by the two inversions, and again the difference is more pronounced in the phase than in apparent resistivity. The response from *ModEM* reproduces the short period phases well but shows small but consistent differences in the overall shape. In comparison, *jif3D* appears to reproduce aspects of the general shape better but does match the phases exactly in any period range.

The observed differences in model fit highlight that different inversion algorithms reproduce different aspects of the observed data that go beyond the changes expected from simply modifying the regularization in a single inversion algorithm. This contrasting behaviour illustrates the value of inverting data with multiple inversion algorithms. It also shows that distortion correction can help fit certain aspects of the data, as demonstrated by the misfit maps, but this does not necessarily imply that all aspects of the data are matched more closely. All in all both inversions with all data match the observations at the majority of sites well. We therefore expect both models to provide reasonable representations of electrical resistivity in the vicinity of the measurements sites.

5 Resistivity models

We show horizontal cross-sections through the derived inversion models between 50 and 200 km depth in 50 km intervals (Figures 8 - 11) as well as vertical slices in the east-west direction at latitude 22° south (Figure 12) and along the Kaapvaal (Figure 13) and Kimberley (Figure 14) profiles (see also Figure 1 for location of these profiles). The

different inversions show very similar large-scale structures, e.g., a generally resistive ($\geq$ 500 Ωm) central region below 50 km depth, which is significantly more resistive than the starting model (100 Ωm). Embedded in this resistive lithosphere are several large conductors, typically associated with boundaries of different geological units. Even though the large-scale picture is similar for all models, there are significant differences in the detailed resistivity structures and values between the inversion results. We will therefore start with a description of the main features based on the "all data" *jif3D* model and discuss how these are expressed in the other models. In the next section, we use the differences and similarities between the models to appraise the robustness and resolution of inversion results.

We observe the maximum resistivity ($\geq$ 5,000 Ωm) around the south-eastern part of the array (labelled the Kaapvaal Resistor (KR) on the horizontal slices) and the north-western part of the array, north of the Damara Conductive Belt (DCB). In both cases, the maximum resistivity is located at depths between 50–100 km and appears to decrease at 150 km depth and below. These observations are compatible with the thick, dry lithospheric mantle associated with the roots of the Kaapvaal Craton and the Congo Craton, respectively (e.g., Evans et al., 2011; Jones et al., 2013; Khoza et al., 2013). In the central part of the array, around latitude 24° south, is a roughly east-west striking band of reduced resistivity ($\sim$100 Ωm) in the deeper slices (150 km and below) which becomes more resistive in the shallower parts of the model. We term the central structure in this band at approximately 24° east the Molopo Farms Conductor (MFC). It can be identified as a zone of decreased resistivity ($<$ 20 Ωm) on the 150 km and 200 km depth slices from the two *ModEM* inversions. The *jif3D* based inversions only show a weak signature at 150 km but show a structure with similarly low resistivity displaced slightly to the north-west at 200 km depth. The conductor associated with Bushveld Complex (Bushveld Conductor, BC) appears on all different modelling schemes north of the Kaapvaal Resistor (KR, Figure 13). Even though its conductivity differs from model to model, less than 10 Ωm in the inversions with *ModEM* and 30–50 Ωm in the inversions with *jif3D* , its spatial extent is consistent between models and it is consistently positioned beneath the surface expression of the Bushveld intrusive complex, suggesting that it is a robustly modelled feature.

Further south, the *ModEM* inversions indicate a low resistivity zone (20 Ωm) at a depth of 50 km near the south-western terminus of the Kaapvaal Craton, which we term

the Southern Kaapvaal Conductor (SKC). The "selected data" *ModEM* inversion shows this low resistivity extending to depths $\geq$ 150 km, but this is less clearly visible in the inversion with all data. Both *jif3D* inversions show decreased resistivities of 100 Ω m compared to the surrounding $1,000\ \Omega m$, but no structures with the low resistivity indicated by *ModEM*.

In the north-western part of the array, the signature of the Damara Conductive Belt (DCB), previously identified by Khoza et al. (2013), is apparent at a depth of 50 km in all inversions. It is an east-west striking band of decreased resistivity ($\sim$10 Ωm), interpreted to be associated with the collision between the Congo Craton and the adjacent mobile belts. At depths of more than 100 km, the inversions with all data also contain an approximately north-south striking, low resistivity feature. The inversions with selected data also show slightly decreased resistivity in the same region, but it appears that some information on this feature is contained in the sites excluded in the selection process.

In addition to these four features discussed above, the model contains a variety of other structures. We do not go into further detail on all these features here but in the second part of this study (Özaydin et al., 2021) we investigate the relationships between the geoelectric lithospheric architecture, composition, tectonic and magmatic history of the southern Africa in detail.

The vertical slices through the model shown in Figures 12 - 14 confirm the inferences made by comparing the horizontal slices, showing similar low and high resistivity features. However, the exact locations, shapes and resistivity values vary between the different inversions. In all cases, the "all data" inversions show stronger resistivity contrasts and more localized features than the "selected data" inversions for the same inversion algorithm, particularly in the upper 50 km. Below this depth, the differences between using all data and selected data are less pronounced, but persist. For example, the *ModEM* "all data" slice along the KAP line (Figure 13) shows a low resistivity zone at a depth of 200 km towards the northern (right) end of the profile. This feature is not clear in the "selected data" inversion, which shows resistivity values comparable with the starting model, possibly suggesting that there is little resolution in this region. Comparing the results from the two different inversion algorithms, *ModEM* appears to favour

more concentrated features at depth while in *jif3D* the features are generally more distributed with less sharp edges.

6 Model appraisal

To provide a quantitative view on the differences between the models, we plot model difference matrices at a depth of 50 km in Figure 15 and 150 km in Figure 16. In both cases, we show a horizontal slice through each model at the respective depth on the diagonal. Plots above the diagonal show the difference in logarithmic resistivity for the different model combinations, while plots below the diagonal show the corresponding resistivity difference histograms. The model histograms show significant differences in resistivity between all model combinations of up to 2 orders of magnitude (2 in logarithmic units), even though for the vast majority of model cells, the difference is less than ± 1 order of magnitude. The histograms appear to be slightly wider at 50 km depth than at 150 km depth. Most histograms are centered around a difference of zero, suggesting that there is no significant overall bias in the resistivities retrieved in each inversion, except the histogram for the two inversions with selected data, which is centered around ≈ 0.2, indicating that the model produced by *jif3D* is consistently more resistive.

The histograms clearly illustrate that the largest resistivity differences are produced by using different algorithms to invert the same dataset, while smaller differences are produced by inverting different subsets of data with the same inversion algorithm. At both depths and for both inversion algorithms, the histograms comparing the "selected" and "all data" inversions show highly symmetric shapes and a concentrated peak at zero, while the other histograms are generally broader and exhibit more structure.

The spatial difference plots in Figures 15 and 16 add more detail to the global resistivity differences displayed in the histograms. Spatial comparisons between the *jif3D* and *ModEM* models using both "selected data" and "all data" datasets at both depths consistently show that the *jif3D* models have higher average resistivities over much of the model space than the *ModEM* models, except for in the south-western part of the array where *jif3D* produces a consistently less resistive model. The south-western region is the part of the model most poorly constrained by station coverage. These differences sum to a resistivity difference histogram that centers on zero. In all difference plots, we also see a correlation between locations of large scale tectonic boundaries and changes

in sign of the resistivity difference, particularly along the northern margin of the Namaqua-Natal Belt and the margins of the Damara and Ghanzi-Chobe belts. While the details vary, this phenomenon is observed in all combinations of models to varying degrees. This indicates that the differences in the models are not merely due to fitting aspects of the data differently or the influence of noisy measurements, but each inversion images the Earth in a different way.

Comparisons between the two "selected data" inversions and the two "all data" inversions demonstrate that data selection has a significant impact on model differences. The spatial difference plots for the *jif3D* and *ModEM* "selected data" inversions reveal broad zones of consistent resistivity differences, while those for the two "all data" inversions show much more inhomogeneous, spatially varying resistivity differences. This results from the stronger influence of regularization in the "selected data" inversions, leading to overall smoother models. When adding data, the wavelength of the patterns decreases, and we see more fine-scaled differences, together with relatively sharp changes between positive and negative differences. Some of the largest differences are located in regions without site coverage, e.g., southeast of the KAP line or in the gaps between measurement lines in the northern part of the array.

The most likely candidate for causing many of these differences is the different regularization schemes. This factor is most clearly seen in the comparison between models produced with the "selected" dataset as the influence of regularization is strongest there. Where the Earth is more resistive than the starting model in both inversions, *jif3D* consistently estimates higher resistivities than *ModEM*. Conversely, where the inversions indicate lower resistivities than the starting model, *jif3D* underestimates resistivity compared to *ModEM* on the larger scale. Both observations can be explained by the fact that *ModEM* minimizes the difference to the reference model and smoothness simultaneously, while *jif3D* only aims at recovering a smooth model. This behaviour can explain the observed correlation between major tectonic boundaries and changes in sign of the resistivity difference. A resistive geological region is likely to be modelled with a higher resistivity in *jif3D* than *ModEM*, and an adjacent conductive geological region is likely to be modelled with a lower resistivity in *jif3D* than *ModEM*. The model difference plot therefore highlights the boundary between these two regions.

Without additional information, we cannot say which of the inversions is more representative of the true resistivity within the Earth. However, we tried to reduce the effect of regularization in *ModEM* by running an additional inversion with a starting and reference model based on laterally smoothed apparent resistivities. To construct this model, for each measurement site we construct a circle with a 4-degree radius centred on the site and take the median apparent resistivity value of all sites within the circle at periods longer than 100 s. The resulting resistivity value is assigned to all cells below this site. We then perform a linear interpolation of logarithmic resistivity between these values to determine the resistivity in each model cell. The resulting model (Figure 17) shows laterally varying resistivities between 50 and 1,000 Ωm and regions of high resistivity that correlate with the most resistive regions identified in the previous inversions.

The resulting median inversion model (Figures 18 and 19) fits the selected data to an RMS comparable with the inversion run from a homogeneous half-space. Compared to the homogeneous inversion run, the average resistivities at 50 km depth (Figure 18) and 150 km depth (Figure 19) are higher, particularly in regions that are not directly covered by sites. Conductive anomalies show a very similar pattern to the previous inversions, although the shape and location differ slightly in some cases, including some of the individual conductors that form the Damara Conductive Belt at 50 km depth (compare Figure 8 and Figure 18) or the Southern Kaapvaal Conductor at 150 km depth. These changes are not significant enough to imply a different geological interpretation of these structures.

The spatial difference plot and difference histogram comparing the median inversion and the inversion of the same data with *jif3D* reveals some interesting changes compared to the inversion with a homogeneous starting model. Visually, the spatial difference plot for the median model contains a lot less long-wavelength structure and is dominated by more small scale differences. This contrast is particularly visible at 50 km depth where *jif3D* previously produced consistently higher resistivities in the central model region. However, the spatial difference plot for the median model displays a much more variable pattern where the sign of the conductivity difference changes within smaller distances. At 150 km depth, the effect is less pronounced yet still observable.

The difference histogram comparing the median inversion and the *jif3D* inversion at 50 km depth has a maximum very close to zero, while the histogram comparing the

homogeneous inversion and *jif3D* is offset to slightly positive values with a maximum at ≈ 0.2. While still not fully symmetric, the maximum and minimum (most negative) differences now show a similar magnitude. At 150 km depth, the impact of the starting model on the histogram is even more pronounced and the median model histogram is more significantly offset to negative values associated with the higher average resistivity of the median model. While the average resistivities inverted from the homogeneous *ModEM* are downward biased compared to *jif3D*, the median model *ModEM* resistivities are upward biased.

7 Discussion and Conclusions

The main goal of this paper is to present a new 3D conductivity model for southern Africa and use the different inversion methodologies to understand uncertainties in the results better. An additional result is that the detailed comparisons of the models also reveal some technical aspects of inversions and regularization that are of interest to both algorithm developers and practitioners and thus warrant some discussion before describing some of the geological interpretations implied by these models.

It is our impression that most of the differences between the results from the two inversion algorithms stem from the different regularization philosophies. The purely smoothness based approach followed by *jif3D* spreads out structures to their maximum possible extent, most clearly visible in Figure 13. Selecting such a smoothing operator has the disadvantage that conductive anomalies can be smeared out, and their boundaries can be challenging to identify. In contrast, the mixed regularization approach pursued by ModEM typically produces more localized structures. On the flip side, the regularization toward a reference model appears to bias the large scale resistivity toward this model, particularly in regions of low sensitivity. This observation is mirrored by the systematic study of Robertson et al. (2020). Taken together, we conclude that for large arrays with heterogeneous coverage such as this, *jif3D* produces models with more representative large-scale resistivity values, while *ModEM* produces more focused and localized anomalies. To some degree, a more representative large-scale resistivity can be obtained with *ModEM* with a median-based starting model, as shown by the comparison at 50 km depth. Still, the shift in bias at 150 km shows that possibly a more detailed starting model with varying resistivity with depth is necessary to obtain good average resistivities over large areas. Alternatively, one could design a regularization scheme where

554 the balance between smoothness and damping toward a reference model can be finely
555 adjusted. While it seems that such an approach could combine the advantages of both
556 regularization approaches, it is questionable how an optimal balance could be objectively
557 found and how practical such a scheme would be for routine application.

558 The effect of inverting for only selected, high-quality data or the maximum amount
559 of data is similar regardless of the inversion algorithm. In both cases, the inclusion of
560 more data increases the misfit of the final models as potentially problematic sites are in-
561 troduced. To some degree, this effect is reduced by the distortion correction employed
562 in *jif3D* which can deal with problems associated with galvanic distortion and achieve
563 a better fit at many sites. At the same time, the models with more data exhibit stronger
564 resistivity contrasts and additional structures, e.g., the north-south striking conductor
565 in the north-western part of the study area that extends from the Congo Craton into the
566 Damara Belt. Given the similarity of these features for both inversion algorithms and
567 the acceptable misfit for the inversion with *jif3D*, we conclude that these are not arte-
568 facts caused by noisy data, but that these features are due to information about the re-
569 sistivity of the Earth contained in the measurements included in the "all data" models.
570 Still, the inversions with selected data contain the same general features as the inver-
571 sions with all data. Based on the similarity with other models and the data fit, our two
572 preferred models are the ones produced by *jif3D* with all data and the *ModEM* inver-
573 sion with a median starting/reference model and selected data.

574 The most prominent features of our two preferred models are: (1) A resistive core
575 of the Kaapvaal Craton as indicated by the Kaapvaal Resistor. This region of high re-
576 sistivity ($> 1,000\Omega m$) extends to depths of 150 km (*ModEM*) to 200 km (*jif3D*) and
577 indicates a dry lithospheric mantle in line with previous 2D interpretations (Evans et al.,
578 2011) and experimental electrical conductivity of common mantle minerals (e.g., Karato
579 & Wang, 2012; Özaydın & Selway, 2020). (2) Other high resistivity regions at depths of
580 100 km and greater include the Congo Craton in the north-west (Kamanjab Inlier) and
581 northern Botswana in the north-eastern part of the array suggesting the presence of litho-
582 sphere with a broadly similar composition in these regions. (3) These resistors are in-
583 tersected by several deep-seated conductors that are present to varying extents in all in-
584 version models. These include the Molopo Farms conductor, the Bushveld conductor and
585 the north-south striking feature below the Congo Craton and Damara Belt. In the lat-
586 ter case, a possible interpretation is a shallower lithosphere-asthenosphere boundary com-

pared to the thick cratonic roots of the Kaapvaal and Congo Cratons (Celli et al., 2020). In contrast, the Molopo Farms Conductor and the Bushveld Conductor are likely expressions of emplacement of metasomatic material during episodes of magmatism (Beukes et al., 2019).

A more detailed interpretation of the resistivity structures recovered by these inversions requires careful consideration of the geological history of the region and the relationships between resistivity, composition and temperature. These considerations are beyond the scope of this study and are presented in a companion paper (Özaydin et al., 2021).

We have constructed a set of 3D models for southern Africa based on two subsets of the SAMTEX magnetotelluric dataset and utilizing two independent inversion algorithms. Despite some differences in the shape of structures and the recovered resistivities, the models show strong similarities. Previous efforts using these data either used the whole dataset but did not perform inversions or were concentrated on regional subsets of the data. Thus the models presented here are the first large-scale resistivity models of the region and can serve as a resource for further investigations and integration with other observations such as gravity and seismology.

Acronyms

BBMT Broad-Band Magnetotelluric

BC Bushveld Conductor

DCB Damara Conductive Belt

MT Magnetotelluric

KR Kaapvaal Resistor

LMT Long-period Magnetotelluric

MFC Molopo Farms Conductor

SAMTEX South African Magnetotelluric Experiment

SKC Southern Kaapvaal Conductor

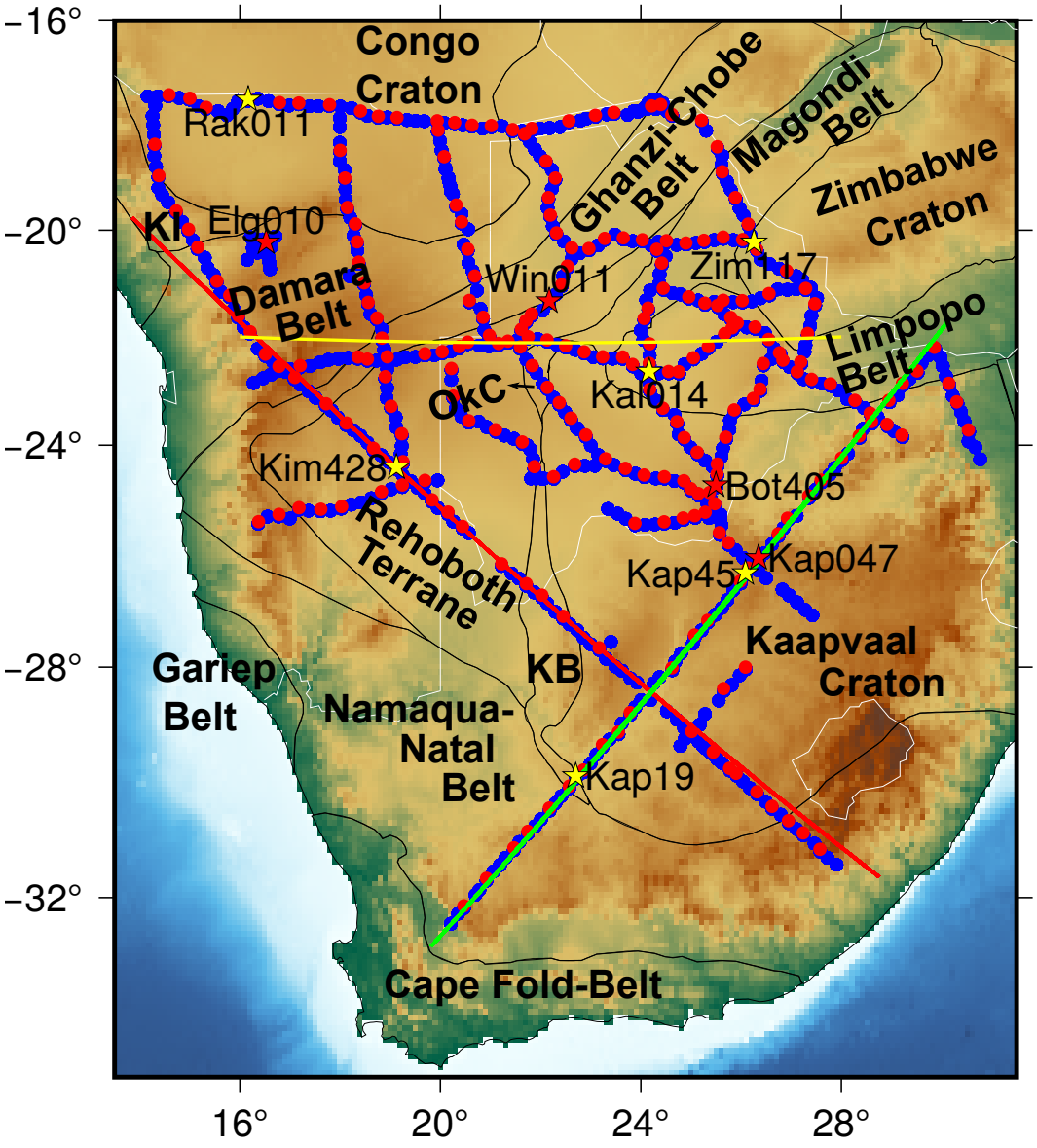

Figure 1. Map of the study area. We show the SAMTEX magnetotelluric measurement sites considered in the full data inversions as blue dots and the sites considered in the inversions with selected data as red dots. Yellow stars indicate exemplary stations for different regions shown in Figure 2 and red stars poor quality data excluded from some of the inversions and shown in Figure 3. The red, green and yellow lines mark the locations of vertical model profiles along the Kimberley, Kaapvaal and 22 degree south lines, respectively. Black lines mark the boundaries of tectonic provinces based on McCourt et al. (2013).

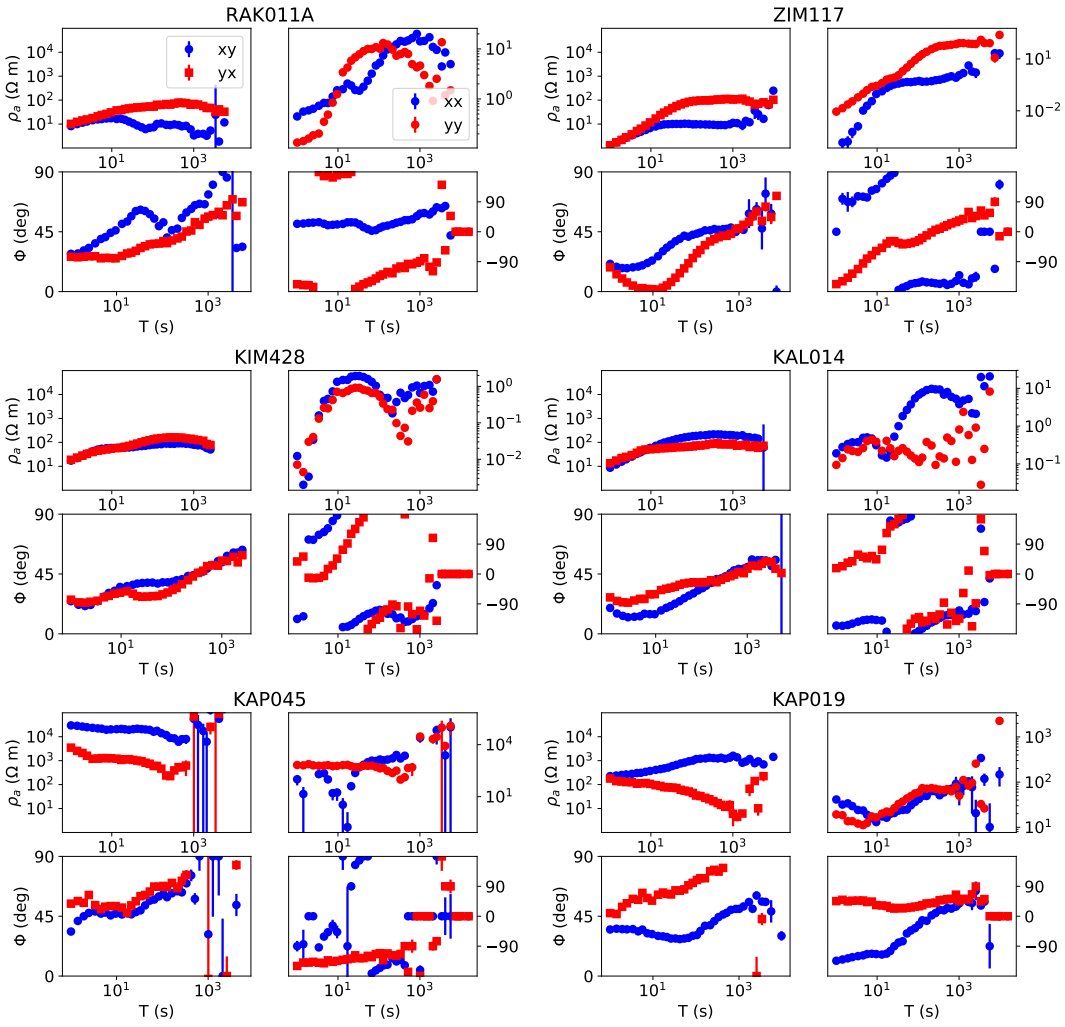

Figure 2. Six exemplary sites representing different regions within the inversion domain. For each site we plot apparent resistivity and phase of the four impedance elements. Off-diagonal (xy and yx) apparent resistivities are plotted with a consistent y-axis to highlight differences in average resistivity between different regions, while apparent resistivity for the diagonal components is plotted with a different scale for each site for better readability.

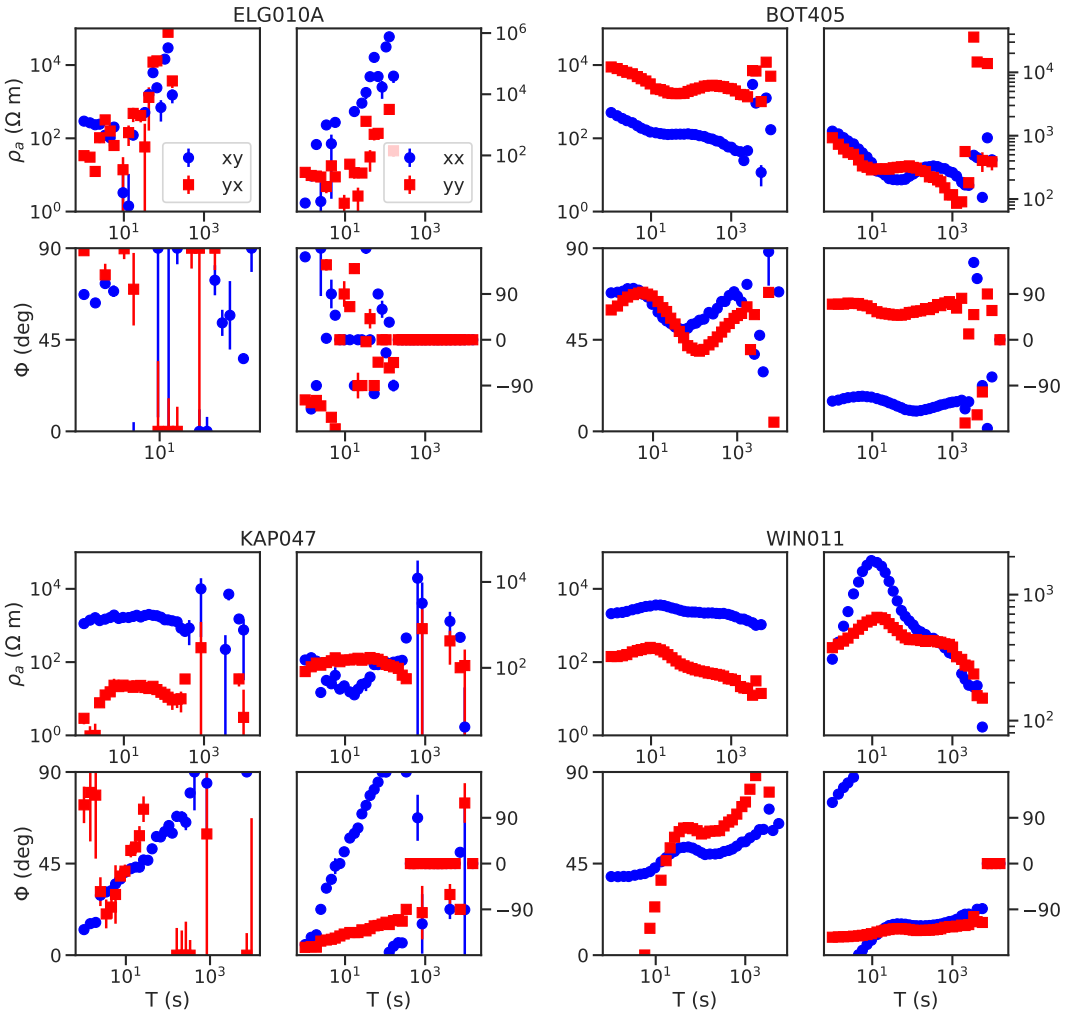

Figure 3. Examples of data excluded from the inversions with selected data. Site ELG10A shows overall problematic data and has been excluded from all inversions while the other sites show potentially problematic features as discussed in the text but have been retained for the inversions with maximum data.

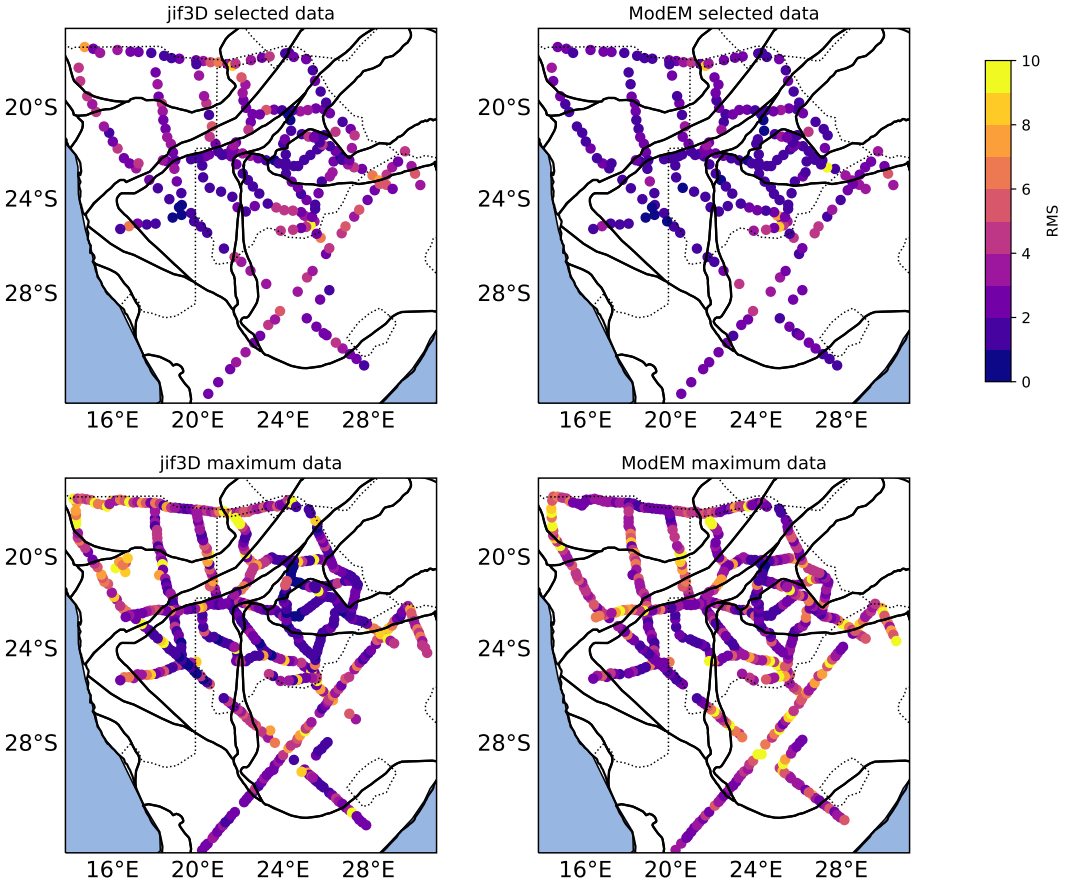

Figure 4. Map of misfit for the four inversion runs. We show the error normalized RMS across all frequencies at each site.

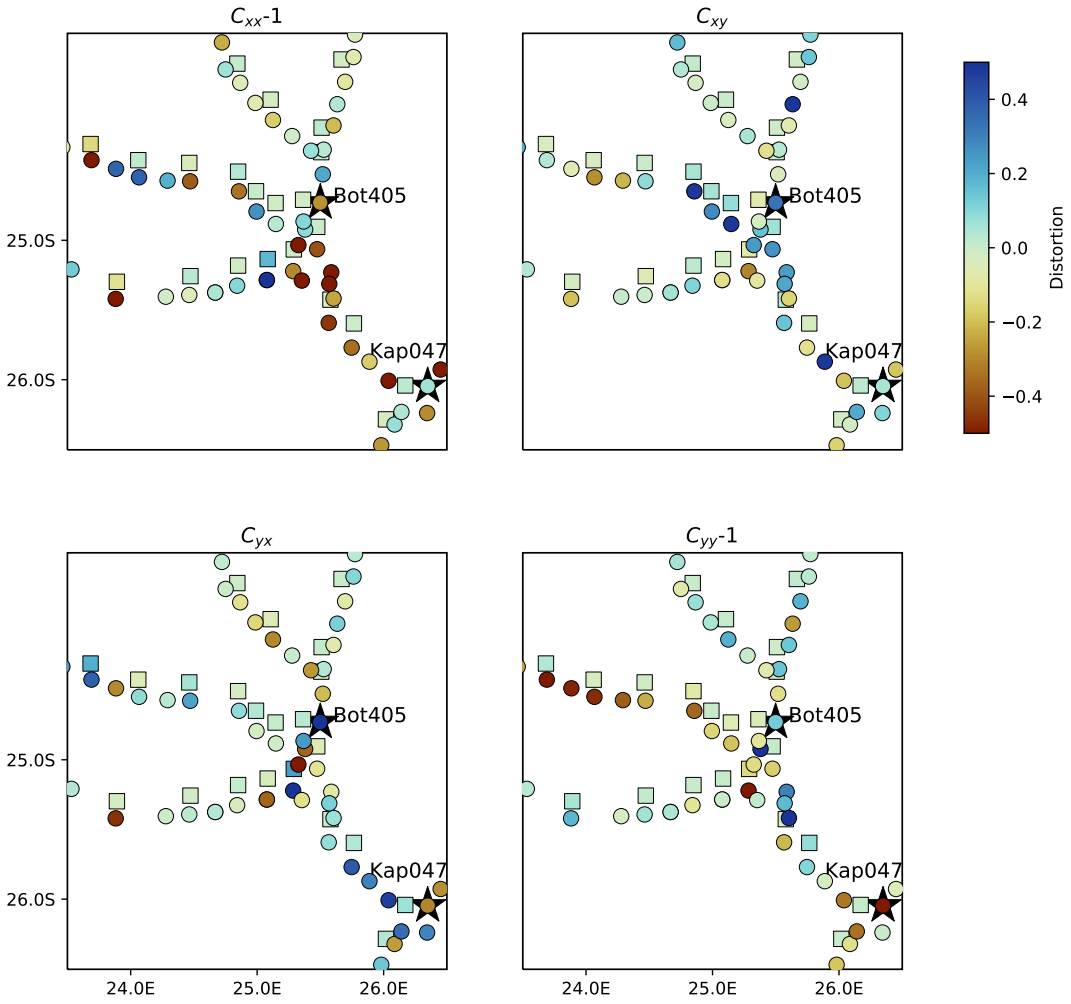

Figure 5. Map of distortion estimates for the inversions with *jif3D* in the central region of the array. We show the estimates for the inversion with all data as circles and for the selected data inversion as squares. These have been displaced north from the original locations for better visibility. Colors mark the deviation of the distortion matrix elements from the identity matrix. We highlight sites BOT405 and KAP047 shown in Figure 3 with black stars.

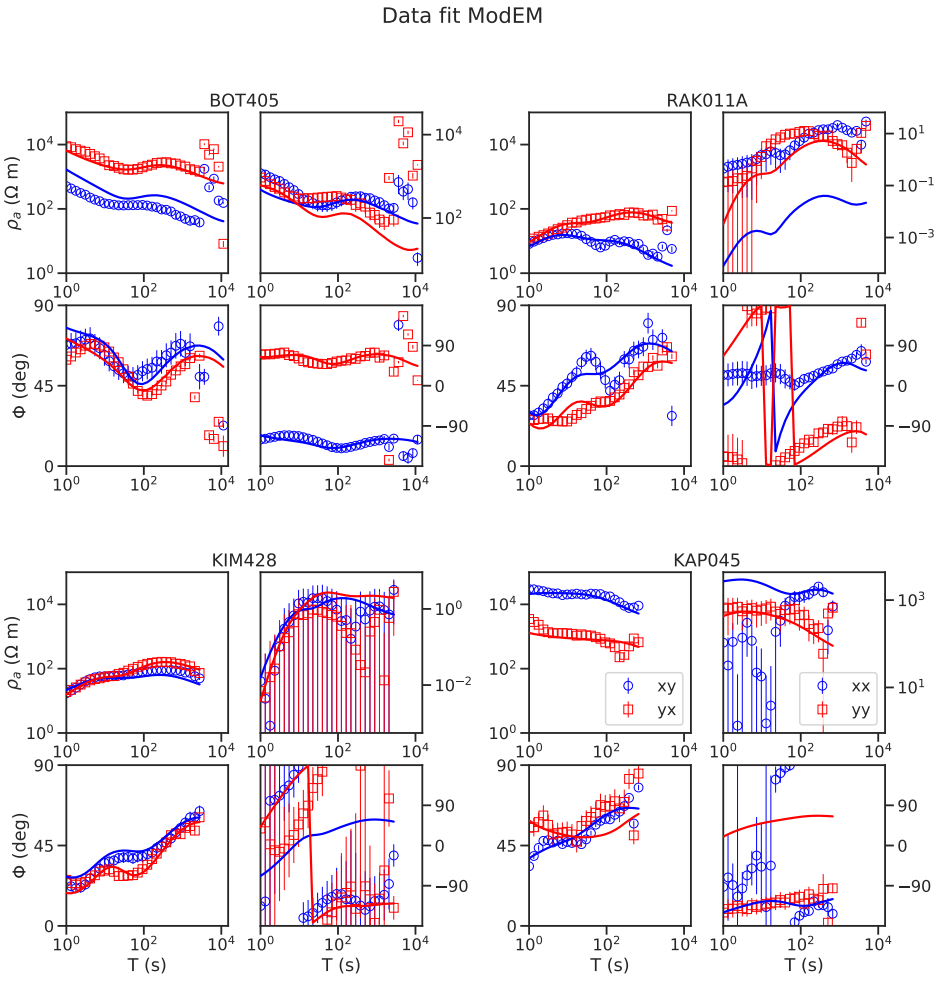

Figure 6. Comparison between observed data (symbols) and predicted data (lines) for the inversion run with *ModEM* and all data for four selected sites marked in Figure 1.

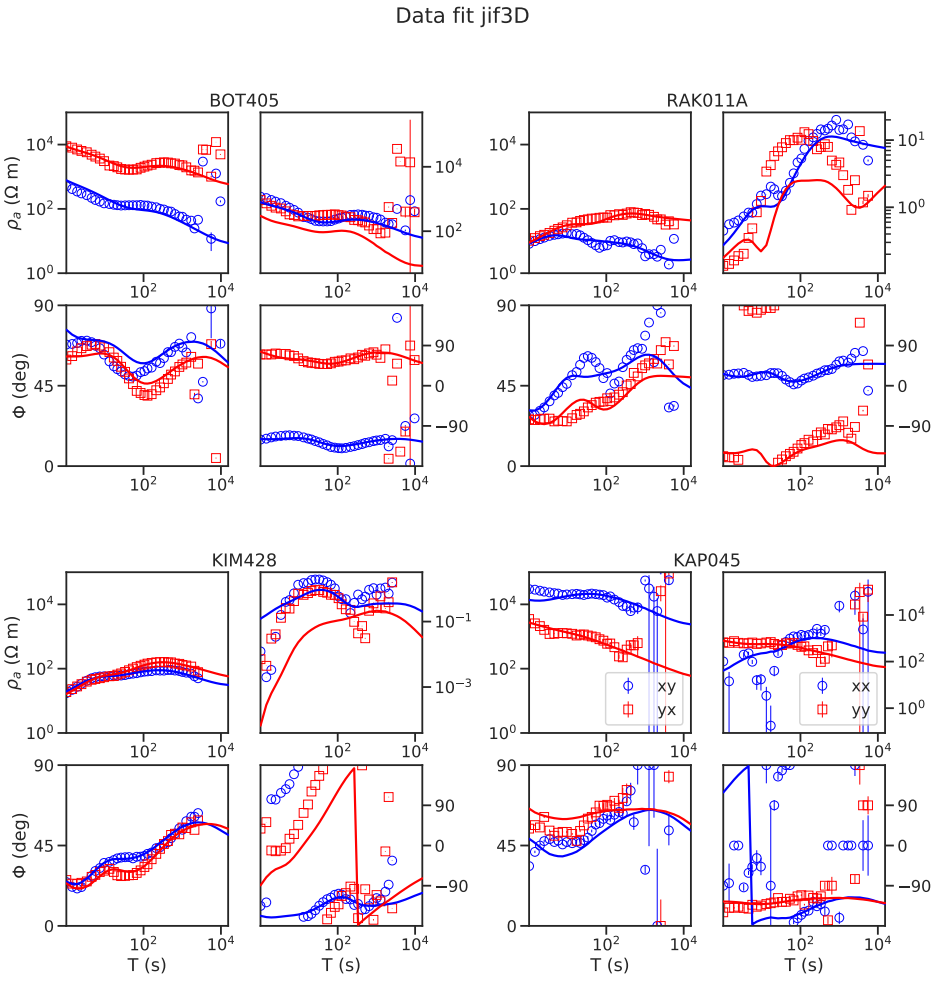

Figure 7. Comparison between observed data (symbols) and predicted data (lines) for the inversion run with *jif3D* and all data for four selected sites marked in Figure 1.

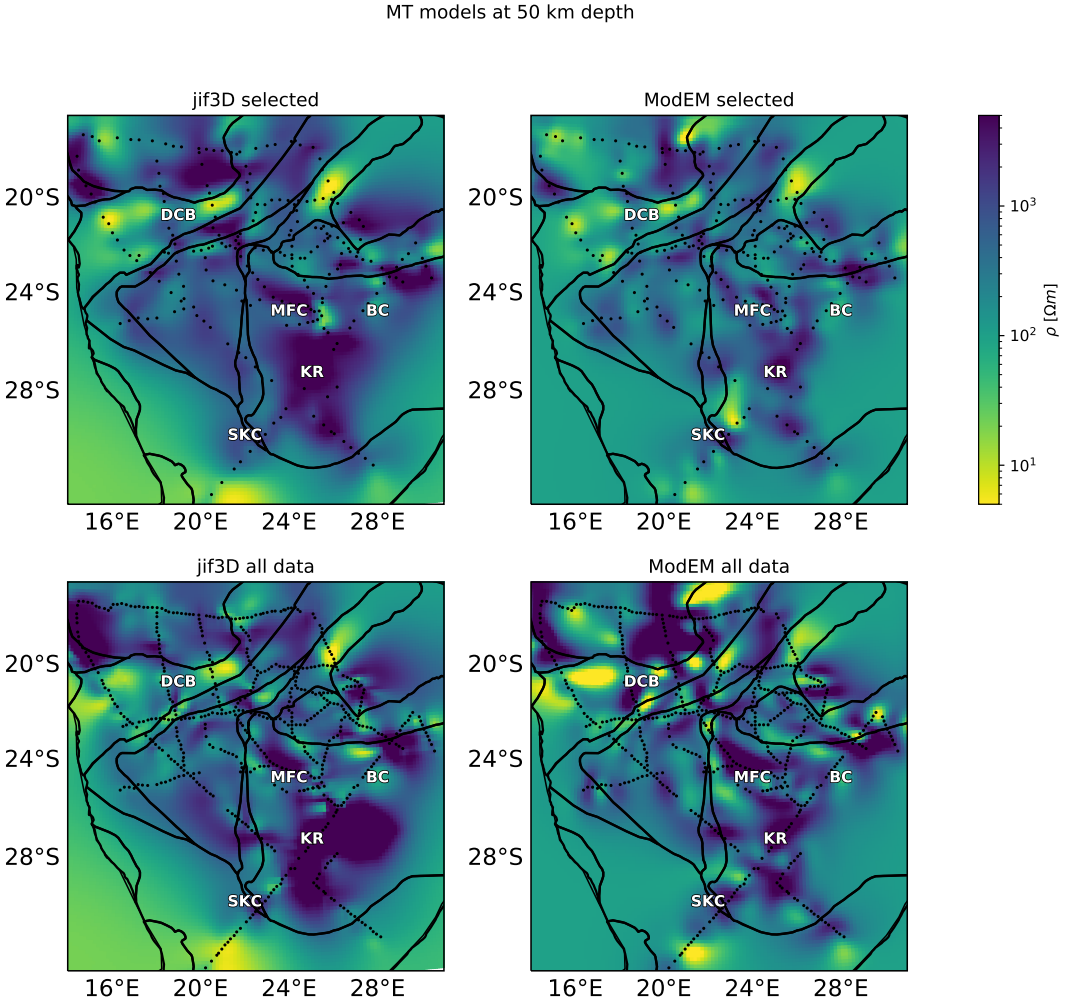

Figure 8. Horizontal slices through the inversion models at a depth of 50 km. We mark several notable structures: Bushveldt Conductor (BC), Damara Conductive Belt (DCB), Kaapvaal Resistor (KR), Molopo Farms Conductor (MFC), Southern Kaapvaal Conductor (SKC).

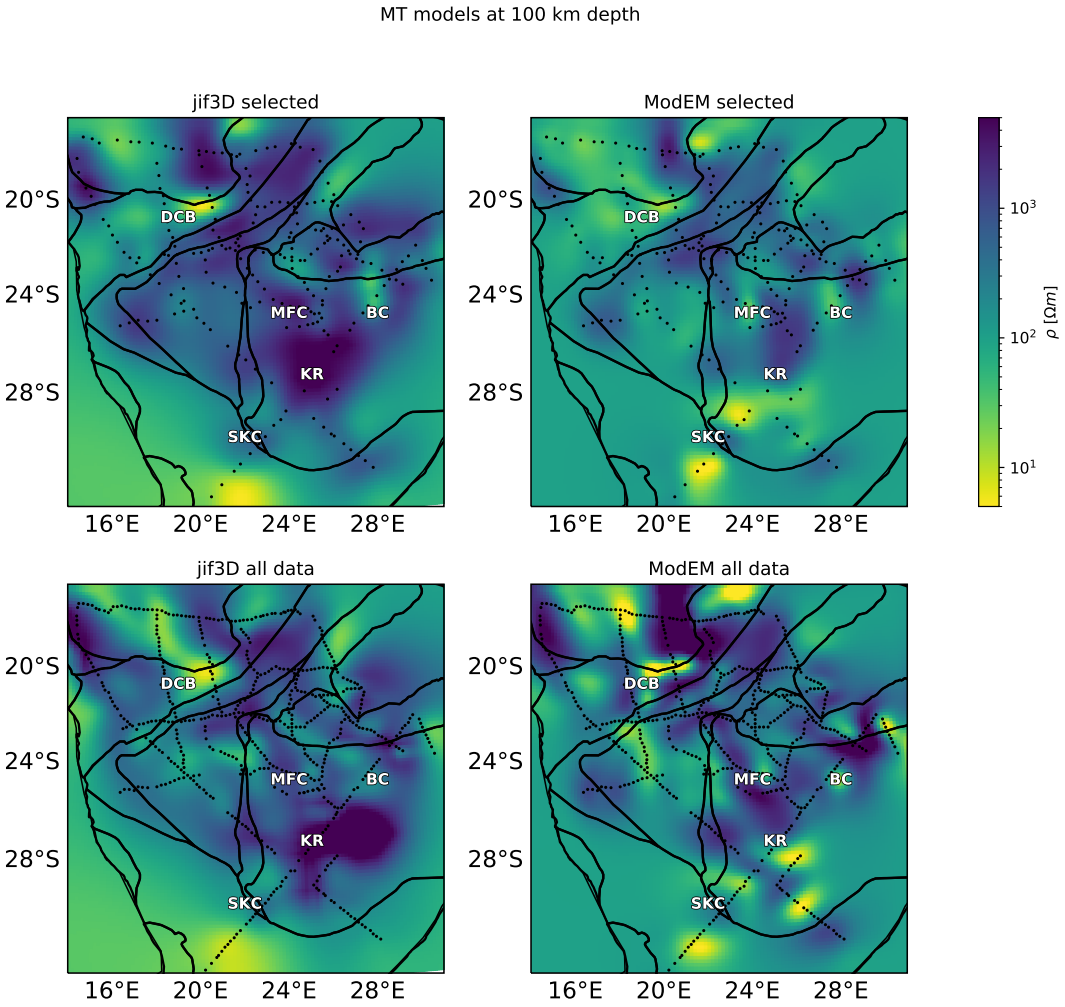

Figure 9. Horizontal slices through the inversion models at a depth of 100 km. For an explanation of abbreviations see Figure 8.

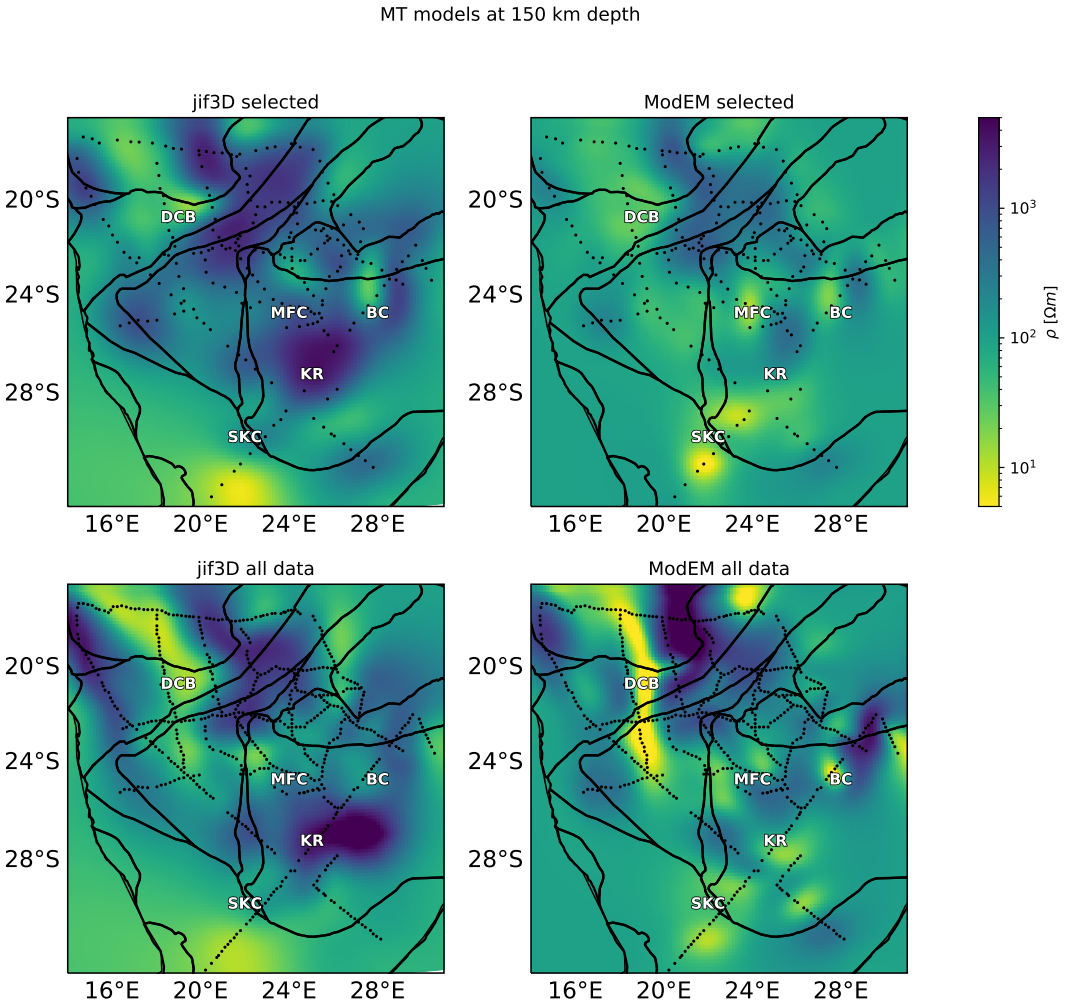

Figure 10. Horizontal slices through the inversion models at a depth of 150 km. For an explanation of abbreviations see Figure 8.

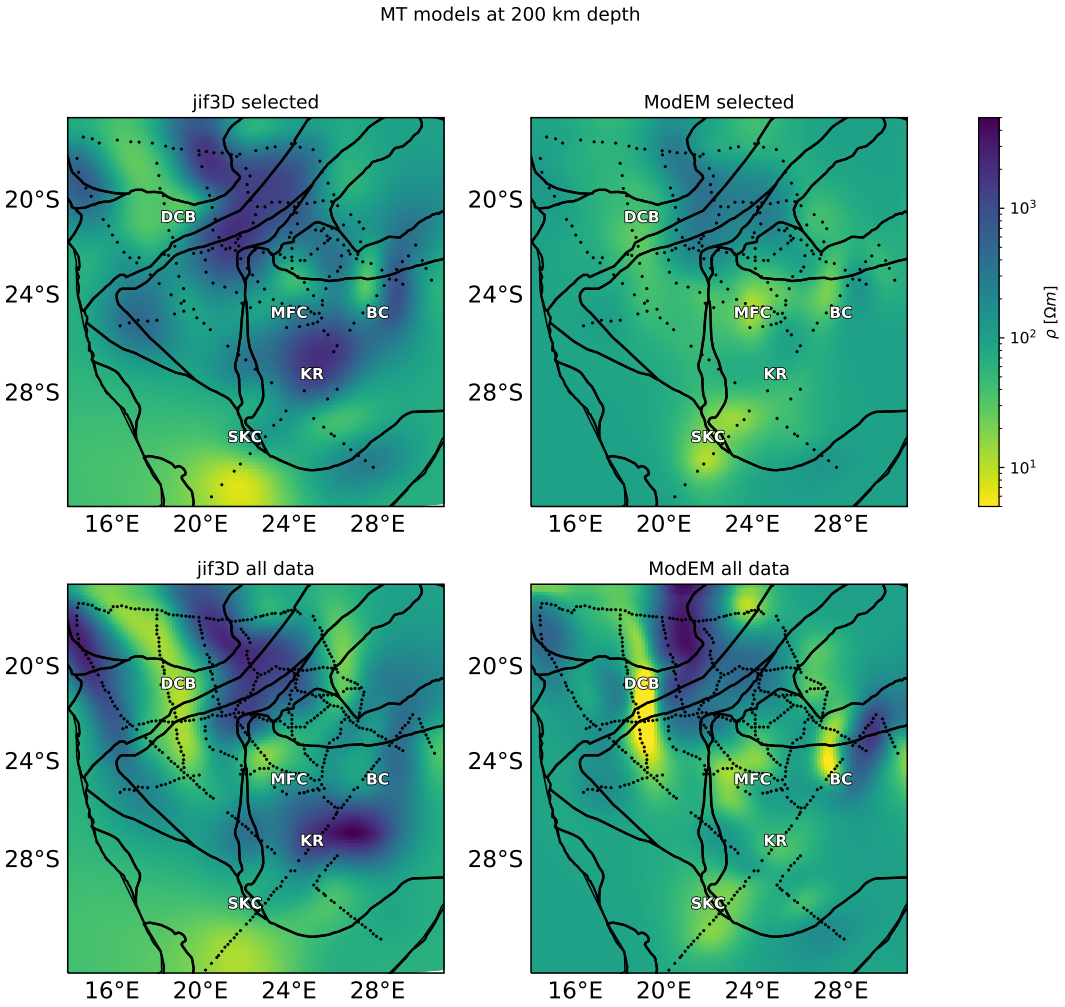

Figure 11. Horizontal slices through the inversion models at a depth of 200 km. For an explanation of abbreviations see Figure 8.

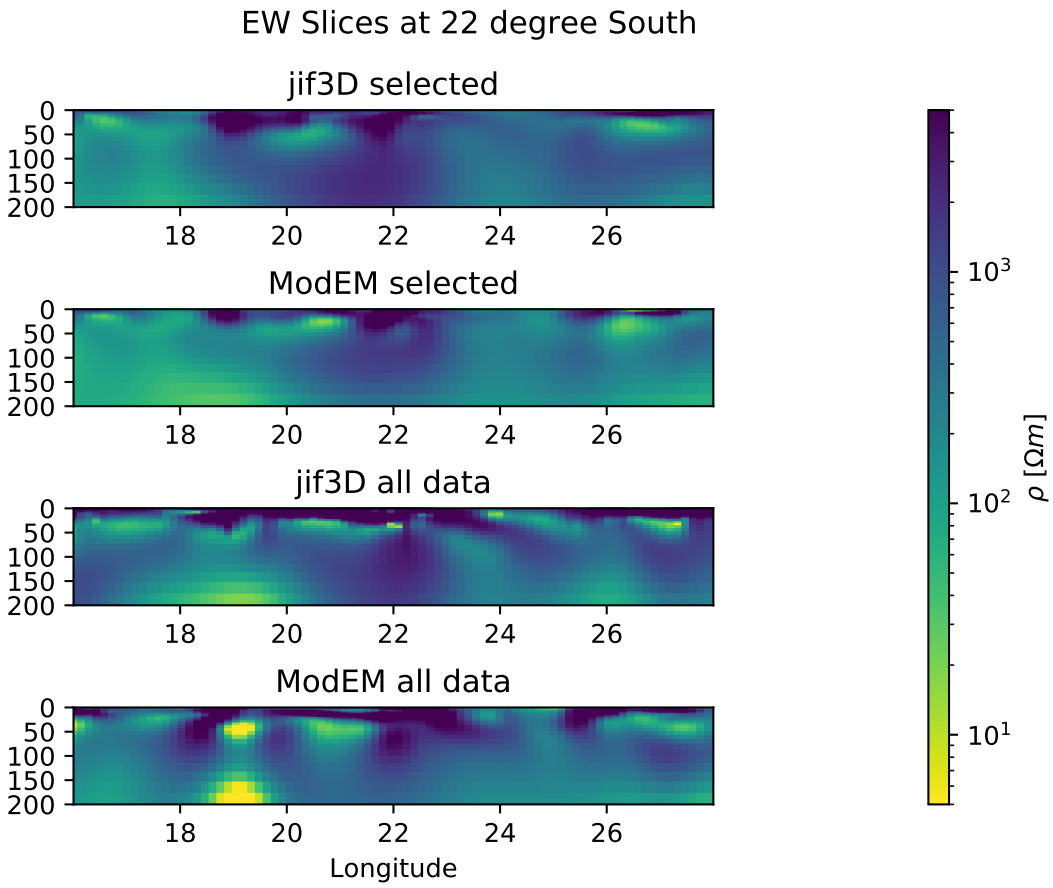

Figure 12. East-west slice through the four inversion models at 22 degree southern latitude (yellow line in Figure 1).

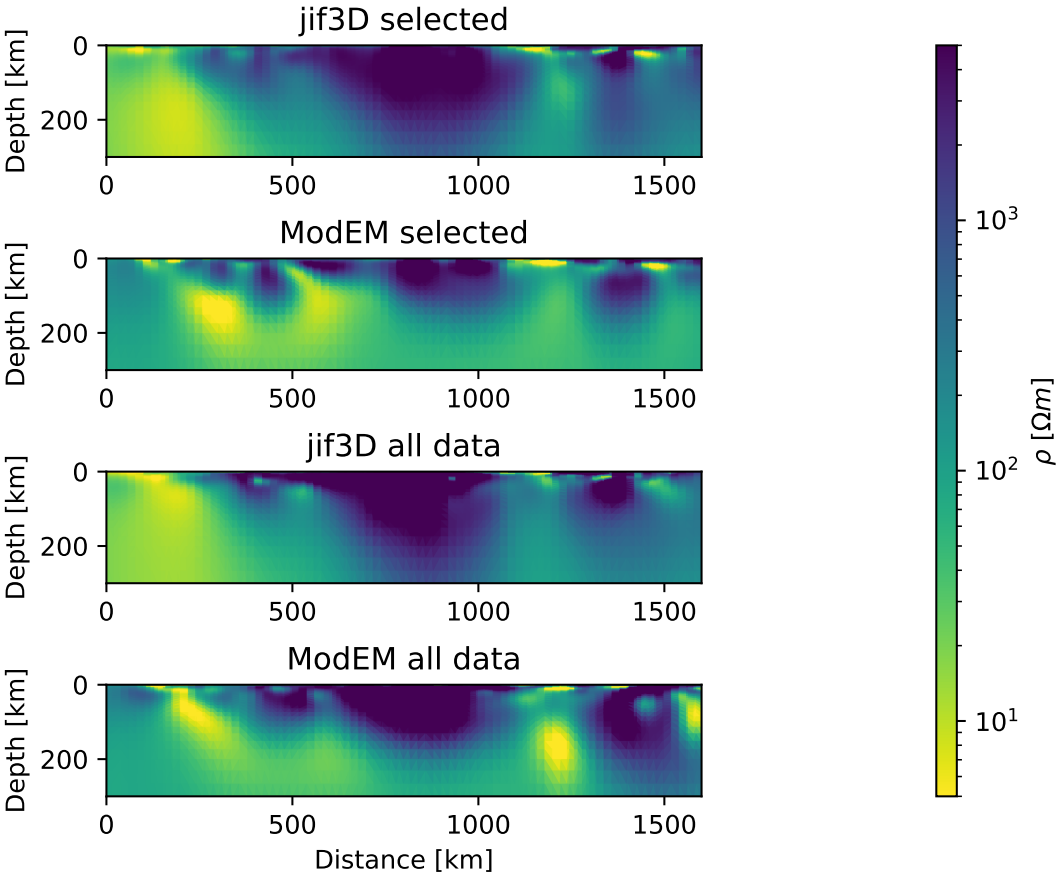

Figure 13. Vertical model slices through the four inversion models along the KAP line (green line in Figure 1). From top to bottom the inversion runs are: *jif3D* with selected data, *ModEM* with selected data, *jif3D* with all data, *ModEM* with all data.

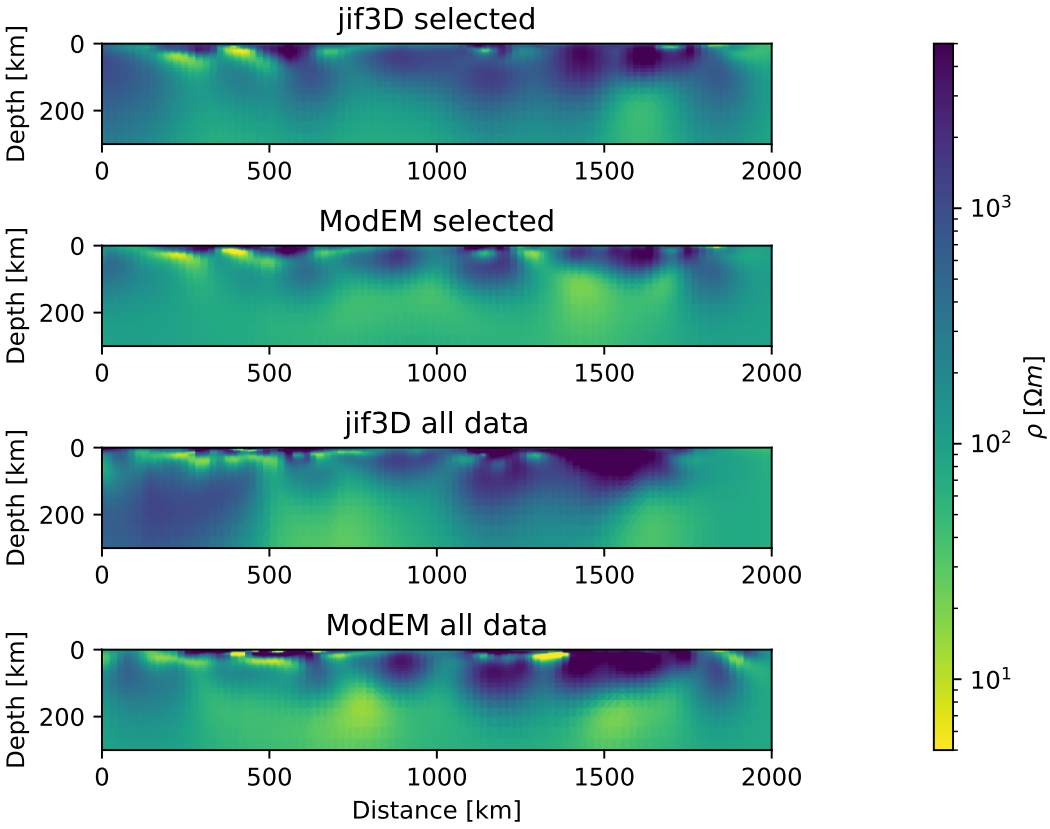

Figure 14. Vertical model slices through the four inversion models along the Kimberley line (red line in Figure 1). From top to bottom the inversion runs are: *jif3D* with selected data, *ModEM* with selected data, *jif3D* with all data, *ModEM* with all data.

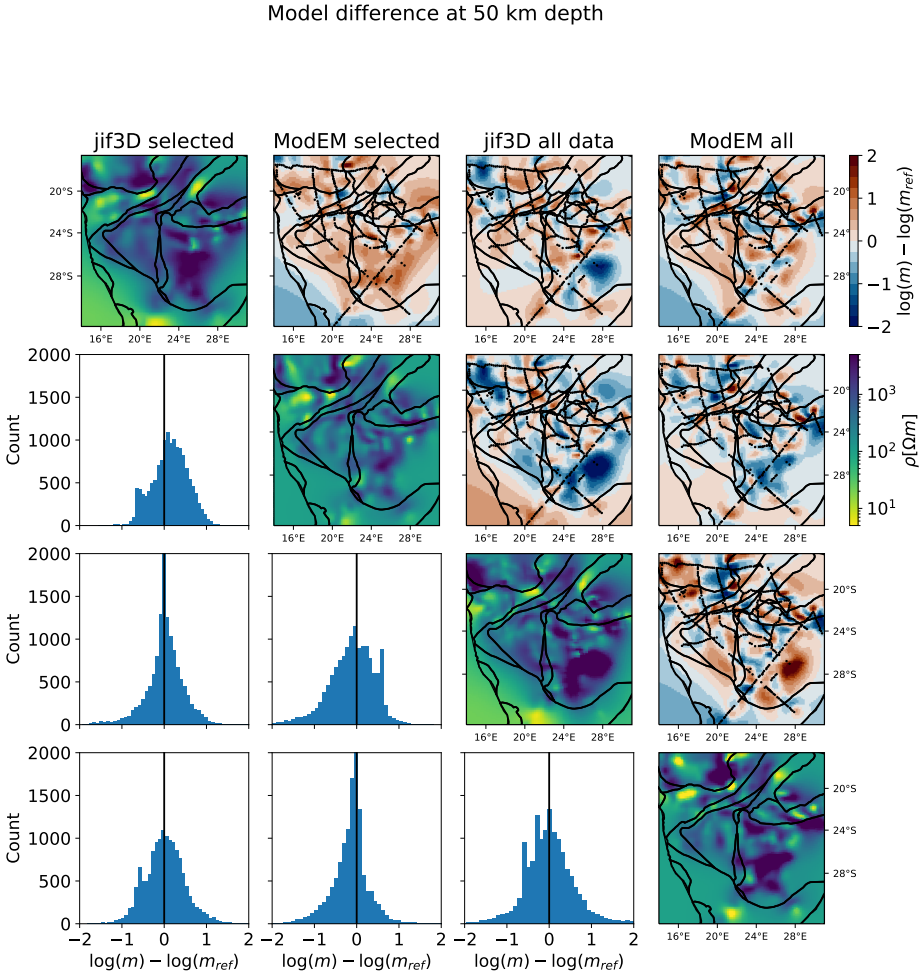

Figure 15. Difference matrix for the four inversion runs at a depth of 50 km. We plot the resistivity slice for each model on the diagonal. Plots above the diagonal show the difference in logarithmic resistivity between pairs of models as labelled above each column, Plots below the diagonal show the corresponding histogram.

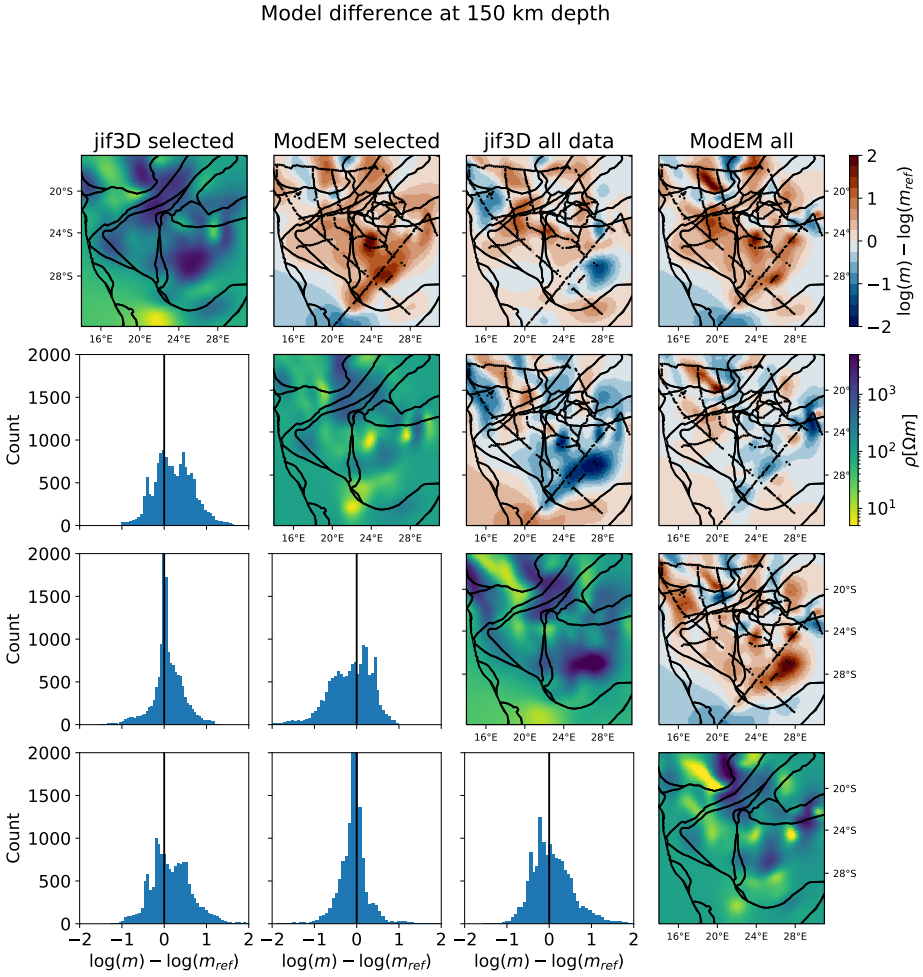

Figure 16. Difference matrix for the four inversion runs at a depth of 150 km. We plot the resistivity slice for each model on the diagonal. Plots above the diagonal show the difference in logarithmic resistivity between pairs of models as labelled above each column, Plots below the diagonal show the corresponding histogram.

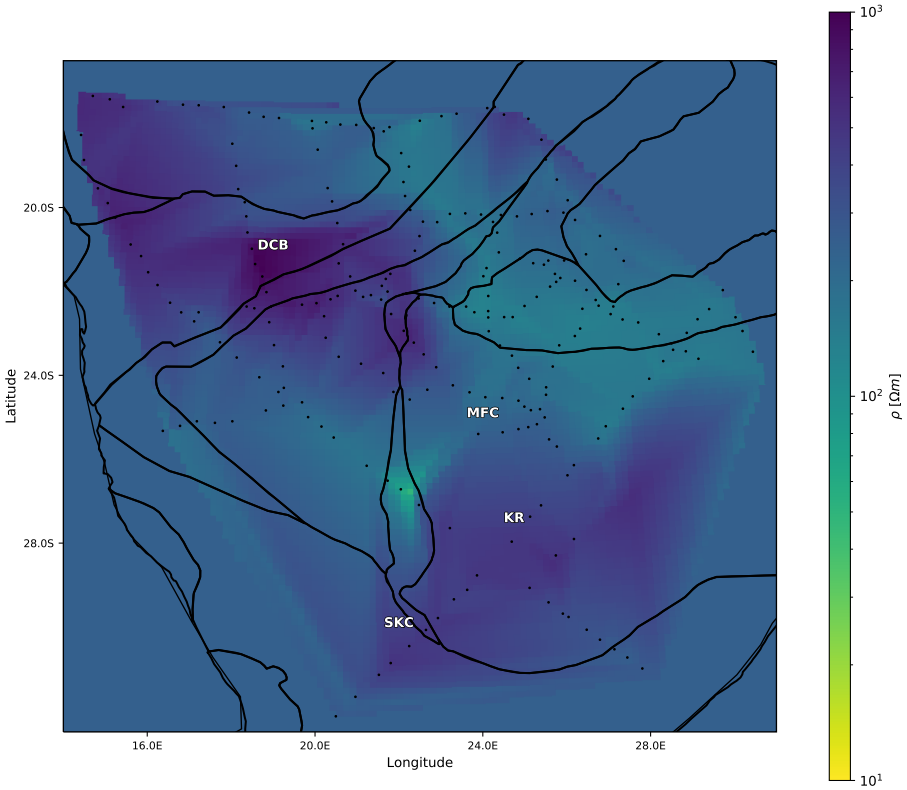

Figure 17. Starting model derived from median apparent resistivity for the inversion with ModEM. Note the reduced range of resistivities in the color bar compared to the other model plots.

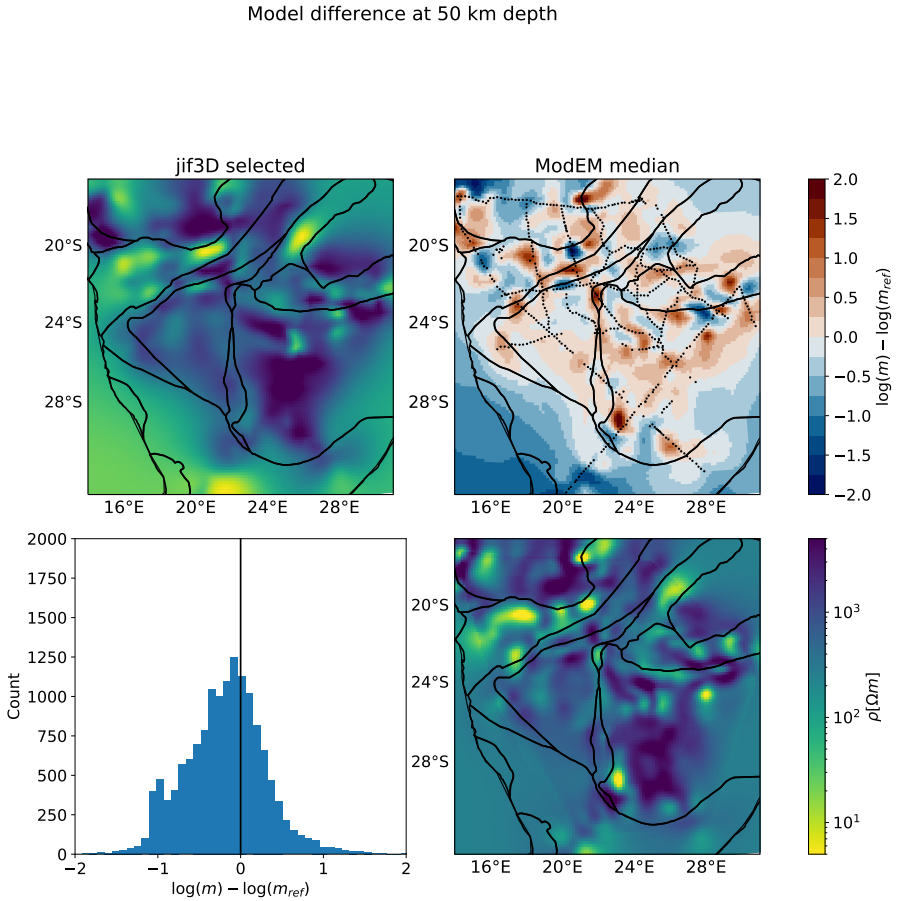

Figure 18. Difference matrix for the ModEM inversion runs with a homogeneous starting model and a median apparent resistivity starting model at a depth of 50 km.

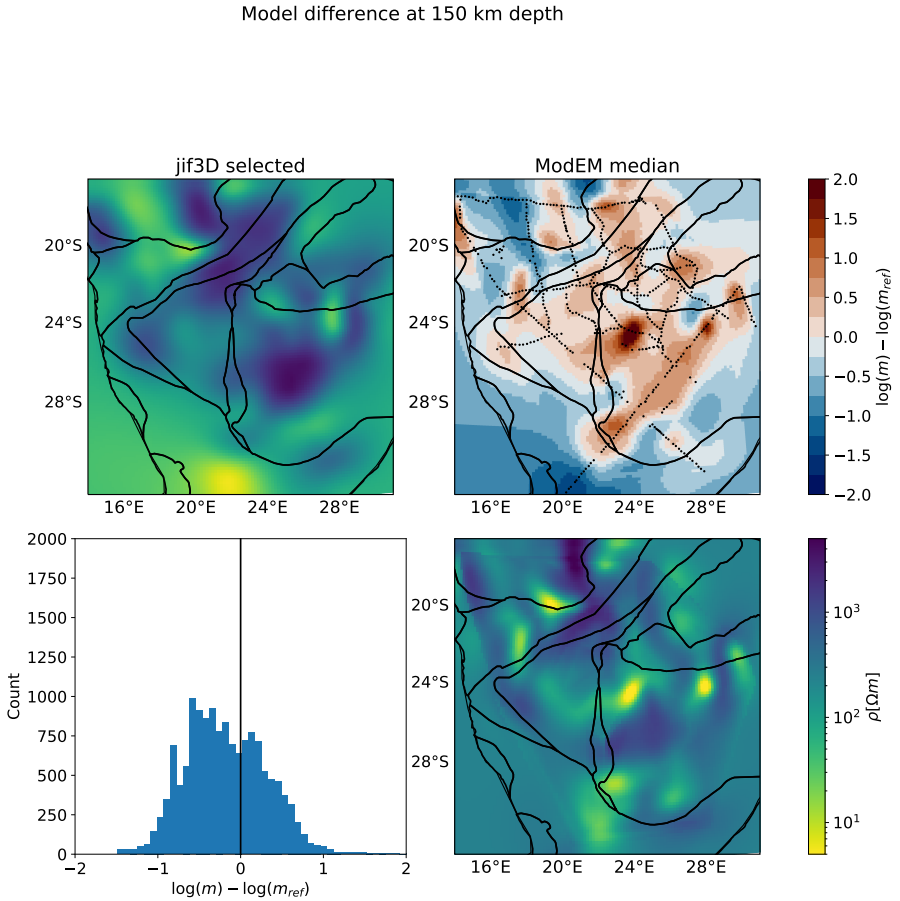

Figure 19. Difference matrix for the ModEM inversion runs with a homogeneous starting model and a median apparent resistivity starting model at a depth of 150 km.

Acknowledgments

MM was funded by the German Research Foundation, DFG, under grant MO 2265/4-1. SÖ and KS are supported by the Australian Research Council grant FT150100541. The SAMTEX magnetotelluric impedance estimates used here are available through the IRIS SPUD repository at `https://doi.org/10.17611/DP/EMTF/SAMTEX`. Download instructions for the ModEM inversion software can be found at `https://sites.google.com/site/modularem/download`. jif3D is available via subversion at `https://svn.code.sf.net/p/jif3d/jif3dsvn/trunk/jif3D`. Figure 1 was prepared using GMT 6.1 (Wessel et al., 2019), all other Figures with Python. We thank Fabio Crameri for designing perceptually uniform color scales used in some of the plots (Crameri et al., 2020).

References

Avdeev, D. B., & Avdeeva, A. (2009). 3d magnetotelluric inversion using a limited-memory quasi-newton optimization. *Geophysics*, *74*(3), F45-F57. doi: 10.1190/1.3114023

Avdeev, D. B., Kuvshinov, A. V., Pankratov, O. V., & Newman, G. A. (1997). High-performance three-dimensional electromagnetic modeling using modified Neumann series. Wide-band numerical solution and examples. *Journal of Geomagnetism and Geoelectricity*, *49*, 1519–1539.

Avdeeva, A., & Avdeev, D. B. (2006). A limited-memory quasi-newton inversion for 1d magnetotellurics. *Geophysics*, *71*(5), G191–G196.

Avdeeva, A., Moorkamp, M., Avdeev, D. B., Jegen, M., & Miensopust, M. (2015). Three-dimensional inversion of magnetotelluric impedance tensor data and full distortion matrix. *Geophysical Journal International*, *202*(1), 464–481.

Begg, G., Griffin, W., Natapov, L., O'Reilly, S. Y., Grand, S., O'Neill, C., ... Deen, T. (2009). The lithospheric architecture of africa: Seismic tomography, mantle petrology, and tectonic evolution. *Geosphere*, *5*(1), 23–50.

Beukes, N. J., de Kock, M. O., Vorster, C., Ravhura, L. G., Frei, D., Gumsley, A. P., & Harris, C. (2019). The age and country rock provenance of the Molopo farms complex: Implications for transvaal supergroup correlation in southern Africa. *South African Journal of Geology*, *122*(1), 39–56. doi: 10.25131/sajg.122.0003

Campanya, J., Ogaya, X., Jones, A. G., Rath, V., Vozar, J., & Meqbel, N. (2016). The advantages of complementing mt profiles in 3-d environments with geomag-

netic transfer function and interstation horizontal magnetic transfer function data: results from a synthetic case study. *Geophysical Supplements to the Monthly Notices of the Royal Astronomical Society*, *207*(3), 1818–1836.

Celli, N. L., Lebedev, S., Schaeffer, A. J., & Gaina, C. (2020). African cratonic lithosphere carved by mantle plumes. *Nature communications*, *11*(1), 1–10.

Chave, A. D., & Jones, A. G. (2012). *The magnetotelluric method*. Cambridge, UK: Cambridge University press.

Chave, A. D., & Thomson, D. J. (2003). A bounded influence regression estimator based on the statistics of the hat matrix. *Journal of the Royal Statistical Society: Series C (Applied Statistics)*, *52*, 307–322.

Clifford, T. N. (1966). Tectono-metallogenic units and metallogenic provinces of africa. *Earth and Planetary Science Letters*, *1*(6), 421–434.

Crameri, F., Shephard, G. E., & Heron, P. J. (2020). The misuse of colour in science communication. *Nature communications*, *11*(1), 1–10.

de Ronde, C. E., & de Wit, M. J. (1994). Tectonic history of the barberton greenstone belt, south africa: 490 million years of archean crustal evolution. *Tectonics*, *13*(4), 983–1005.

De Wit, M. J., de Ronde, C. E., Tredoux, M., Roering, C., Hart, R. J., Armstrong, R. A., ... Hart, R. A. (1992). Formation of an archaean continent. *Nature*, *357*(6379), 553–562.

Dong, H., Wei, W., Jin, S., Ye, G., Jones, A. G., Zhang, L., ... Yin, Y. (2020). Shaping the surface deformation of central and south tibetan plateau: Insights from magnetotelluric array data. *Journal of Geophysical Research: Solid Earth*, *125*(9), e2019JB019206.

Dong, S.-W., Li, T.-D., Lü, Q.-T., Gao, R., Yang, J.-S., Chen, X.-H., ... Zhou, Q. (2013). Progress in deep lithospheric exploration of the continental china: A review of the sinoprobe. *Tectonophysics*, *606*, 1–13.

Egbert, G., & Kelbert, A. (2012). Computational recipes for electromagnetic inverse problems. *Geophysical Journal International*, *189*(1), 251-267.

Evans, R. L., Jones, A. G., Garcia, X., Muller, M., Hamilton, M., Evans, S., ... Jelsma, H. (2011). Electrical lithosphere beneath the Kaapvaal craton, southern Africa. *Journal of Geophysical Research: Solid Earth*, *116*(B4).

Field, M., Stiefenhofer, J., Robey, J., & Kurszlaukis, S. (2008). Kimberlite-hosted

diamond deposits of southern africa: a review. *Ore Geology Reviews*, *34*(1-2), 33–75.

Finn, C. A., Bedrosian, P. A., Cole, J. C., Khoza, T. D., & Webb, S. J. (2015). Mapping the 3d extent of the northern lobe of the bushveld layered mafic intrusion from geophysical data. *Precambrian Research*, *268*, 279–294.

Fouch, M. J., James, D. E., VanDecar, J. C., Van der Lee, S., & Group, K. S. (2004). Mantle seismic structure beneath the kaapvaal and zimbabwe cratons. *South African Journal of Geology*, *107*(1-2), 33–44.

Fullea, J., Muller, M., & Jones, A. G. (2011). Electrical conductivity of continental lithospheric mantle from integrated geophysical and petrological modeling: Application to the Kaapvaal Craton and Rehoboth Terrane, southern Africa. *Journal of Geophysical Research: Solid Earth*, *116*(B10).

Gatzemeier, A., & Moorkamp, M. (2005). 3d modelling of electrical anisotropy from electromagnetic array data: hypothesis testing for different upper mantle conduction mechanisms. *Physics of the Earth and Planetary Interiors*, *149*, 225-242.

Grégoire, M., Bell, D., & Le Roex, A. (2003). Garnet lherzolites from the kaapvaal craton (south africa): trace element evidence for a metasomatic history. *Journal of Petrology*, *44*(4), 629–657.

Griffin, W., O'Reilly, S., Afonso, J., & Begg, G. (2009). The composition and evolution of lithospheric mantle: A re-evaluation and its tectonic implications. *Journal of Petrology*, *50*(7), 1185-1204.

Griffin, W., O'Reilly, S. Y., Natapov, L., & Ryan, C. (2003). The evolution of lithospheric mantle beneath the kalahari craton and its margins. *Lithos*, *71*(2-4), 215–241.

Hamilton, M., Jones, A. G., Evans, R. L., Evans, S., Fourie, C. J. S., Garcia, X., ... the SAMTEX Team (2006). Electrical anisotropy of South African lithosphere compared with seismic anisotropy from shear-wave splitting analysis. *Physics of the Earth and Planetary Interiors*, *158*, 226-239.

Jones, A. G. (1999). Imaging the continental upper mantle using electromagnetic methods. *Lithos*, *48*(1-4), 57–80.

Jones, A. G., Evans, R. L., Muller, M. R., Hamilton, M. P., Miensopust, M. P., Garcia, X., ... The SAMTEX Team (2009). Area selection for diamonds using magnetotellurics: Examples from southern africa. *Lithos*, *112*, 83–92.

Jones, A. G., Fishwick, S., Evans, R., Muller, M., & Fullea, J. (2013). Velocity-conductivity relations for cratonic lithosphere and their application: Example of Southern Africa. *Geochemistry, Geophysics, Geosystems*, *14*(4), 806-827.

Jones, A. G., Fullea, J., Evans, R., & Muller, M. (2012). Water in cratonic lithosphere: Calibrating laboratory-determined models of electrical conductivity of mantle minerals using geophysical and petrological observations. *Geochemistry, Geophysics, Geosystems*, *13*(6).

Karato, S.-i., & Wang, D. (2012). Electrical conductivity of minerals and rocks. *Physics and Chemistry of the Deep Earth*, 145–236.

Kelbert, A. (2019). Taking magnetotelluric data out of the drawer. *AGUFM*, *2019*, IN21A–01.

Kelbert, A., & Egbert, G. (2012). Crust and upper mantle electrical conductivity beneath the Yellowstone Hotspot Track. *Geology*, *40*(5), 447–450.

Kelbert, A., Meqbel, N., Egbert, G. D., & Tandon, K. (2014). ModEM: A modular system for inversion of electromagnetic geophysical data. *Computers and Geosciences*, *66*, 40–53. doi: 10.1016/j.cageo.2014.01.010

Kennedy, M. C., & O'Hagan, A. (2001). Bayesian calibration of computer models. *Journal of the Royal Statistical Society: Series B (Statistical Methodology)*, *63*(3), 425–464.

Khoza, T. D., Jones, A. G., Muller, M. R., Evans, R. L., Miensopust, M. P., & Webb, S. J. (2013). Lithospheric structure of an Archean craton and adjacent mobile belt revealed from 2-D and 3-D inversion of magnetotelluric data: Example from southern Congo Craton in northern Namibia. *Journal of Geophysical Research: Solid Earth*, *118*(8), 4378–4397.

Kirkby, A. L., Musgrave, R. J., Czarnota, K., Doublier, M. P., Duan, J., Cayley, R. A., & Kyi, D. (2020). Lithospheric architecture of a phanerozoic orogen from magnetotellurics: Auslamp in the tasmanides, southeast australia. *Tectonophysics*, *793*, 228560.

Kobussen, A. F., Griffin, W. L., & O'Reilly, S. Y. (2009). Cretaceous thermochemical modification of the kaapvaal cratonic lithosphere, south africa. *Lithos*, *112*, 886–895.

Lee, C.-T. A., Luffi, P., & Chin, E. J. (2011). Building and destroying continental mantle. *Annual Review of Earth and Planetary Sciences*, *39*, 59–90.

Mackie, R., Smith, J., & Madden, T. (1994). Three-dimensional electromagnetic modeling using finite difference equations: The magnetotelluric example. *Radio Science*, *29*, 923-935.

McCourt, S., Armstrong, R. A., Jelsma, H., & Mapeo, R. B. (2013). New U-Pb SHRIMP ages from the Lubango region, SW Angola: Insights into the Palaeoproterozoic evolution of the Angolan Shield, southern Congo Craton, Africa. *Journal of the Geological Society*, *170*(2), 353–363. doi: 10.1144/jgs2012-059

Meqbel, N. M., Egbert, G. D., Wannamaker, P. E., Kelbert, A., & Schultz, A. (2014). Deep electrical resistivity structure of the northwestern US derived from 3-d inversion of USArray magnetotelluric data. *Earth and Planetary Science Letters*, *402*, 290–304.

Miensopust, M. P. (2017). Application of 3-d electromagnetic inversion in practice: Challenges, pitfalls and solution approaches. *Surveys in Geophysics*, *38*(5), 869–933.

Miensopust, M. P., Jones, A. G., Muller, M. R., Garcia, X., & Evans, R. L. (2011). Lithospheric structures and precambrian terrane boundaries in northeastern Botswana revealed through magnetotelluric profiling as part of the Southern African Magnetotelluric Experiment. *Journal of Geophysical Research: Solid Earth*, *116*(B2).

Moorkamp, M., Avdeeva, A., Basokur, A. T., & Erdogan, E. (2020). Inverting magnetotelluric data with distortion correction—stability, uniqueness and trade-off with model structure. *Geophysical Journal International*, *222*(3), 1620-1638. doi: 10.1093/gji/ggaa278

Moorkamp, M., Fishwick, S., Walker, R. J., & Jones, A. G. (2019). Geophysical evidence for crustal and mantle weak zones controlling intra-plate seismicity–the 2017 Botswana earthquake sequence. *Earth and Planetary Science Letters*, *506*, 175–183.

Moorkamp, M., Heincke, B., Jegen, M., Roberts, A. W., & Hobbs, R. W. (2011). A framework for 3-D joint inversion of MT, gravity and seismic refraction data. *Geophysical Journal International*, *184*, 477-493. doi: 10.1111/j.1365-246X.2010.04856.x

Muller, M., Jones, A. G., Evans, R., Grütter, H., Hatton, C., Garcia, X., ... Ngwisanyi, T. (2009). Lithospheric structure, evolution and diamond prospectivity

of the rehoboth terrane and western kaapvaal craton, southern africa: Constraints from broadband magnetotellurics. *Lithos*, *112*, 93–105.

Özaydin, S., Selway, K., Griffin, W., & Moorkamp, M. (2021). Composition of the southern african lithospheric mantle and its relevance to magnetotelluric models. *Journal of Geophysical Research*, *submitted*.

Özaydın, S., & Selway, K. (2020). MATE: An analysis tool for the interpretation of magnetotelluric models of the mantle. *Geochemistry, Geophysics, Geosystems*, 1–26. doi: 10.1029/2020gc009126

Özaydın, S., Selway, K., & Griffin, W. L. (2021). Are xenoliths from southwestern Kaapvaal Craton representative of the broader mantle? Constraints from magnetotelluric modeling. *Geophysical Research Letters*, *48*, 1–11. doi: 10.1029/2021GL092570

Pearce, R., Sánchez de la Muela, A., Moorkamp, M., Hammond, J. O., Mitchell, T., Cembrano, J., ... Pérez Estay, N. (2020). Reactivation of fault systems by compartmentalized hydrothermal fluids in the southern andes revealed by magnetotelluric and seismic data. *Tectonics*, e2019TC005997.

Rao, C., Jones, A. G., Moorkamp, M., & Weckmann, U. (2014). Implications for the lithospheric geometry of the iapetus suture beneath ireland based on electrical resistivity models from deep-probing magnetotellurics. *Geophysical Journal International*, *198*(2), 737–759.

Robertson, K., Heinson, G., & Thiel, S. (2016). Lithospheric reworking at the proterozoic–phanerozoic transition of australia imaged using auslamp magnetotelluric data. *Earth and Planetary Science Letters*, *452*, 27–35.

Robertson, K., Thiel, S., & Meqbel, N. (2020). Quality over quantity: On workflow and model space exploration of 3d inversion of MT data. *Earth, Planets and Space*, *72*(1), 1–22.

Selway, K. (2014). On the causes of electrical conductivity anomalies in tectonically stable lithosphere. *Surveys in Geophysics*, *35*(1), 219–257.

Selway, K. (2018). Electrical discontinuities in the continental lithosphere imaged with magnetotellurics. *Lithospheric discontinuities*, 89–109.

Selway, K., Ford, H., & Kelemen, P. (2015). The seismic mid-lithosphere discontinuity. *Earth and Planetary Science Letters*, *414*, 45–57.

Sodoudi, F., Yuan, X., Kind, R., Lebedev, S., Adam, J. M.-C., Kästle, E., &

Tilmann, F. (2013). Seismic evidence for stratification in composition and anisotropic fabric within the thick lithosphere of kalahari craton. *Geochemistry, Geophysics, Geosystems*, *14*(12), 5393–5412.

Thiel, S., Goleby, B. R., Pawley, M. J., & Heinson, G. (2020). Auslamp 3d mt imaging of an intracontinental deformation zone, musgrave province, central australia. *Earth, Planets and Space*, *72*(1), 1–21.

VanTongeren, J. A. (2018). Mixing and unmixing in the bushveld complex magma chamber. *Processes and Ore Deposits of Ultramafic-Mafic Magmas through Space and Time*, 113–138.

Wannamaker, P., Hill, G., Stodt, J., Maris, V., Ogawa, Y., Selway, K., ... Ayling, B. (2017). Uplift of the central transantarctic mountains. *Nature communications*, *8*(1), 1–11.

Wessel, P., Luis, J., Uieda, L., Scharroo, R., Wobbe, F., Smith, W., & Tian, D. (2019). The generic mapping tools version 6. *Geochemistry, Geophysics, Geosystems*, *20*(11), 5556–5564.

White-Gaynor, A., Nyblade, A., Durrheim, R., Raveloson, R., van der Meijde, M., Fadel, I., ... Titus, N. (2020). Lithospheric boundaries and upper mantle structure beneath southern africa imaged by p and s wave velocity models. *Geochemistry, Geophysics, Geosystems*, *21*(10), e2020GC008925.